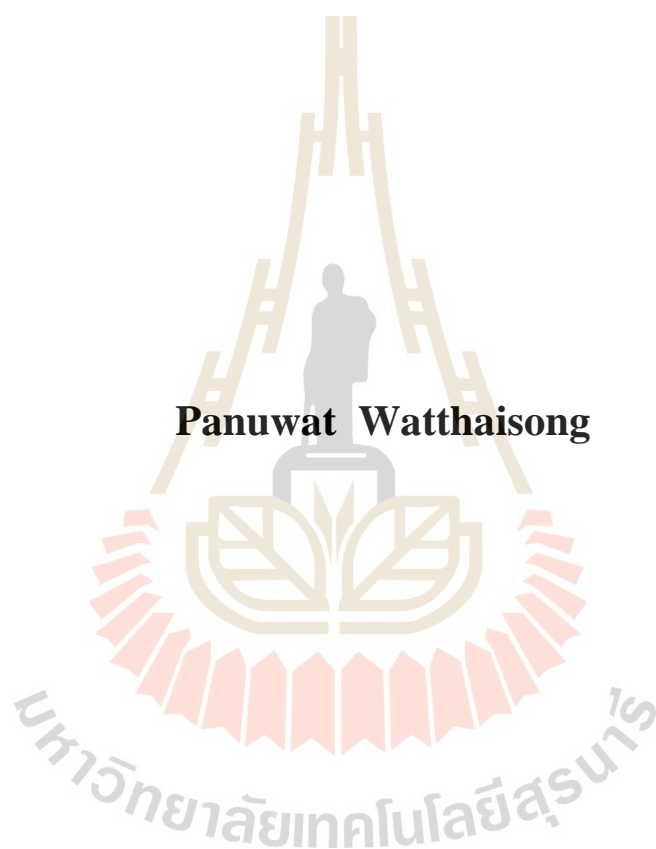# MECHANISTIC STUDY OF ETHYLENE CARBONATE DECOMPOSITION ON CARBON ANODE OF SODIUM-ION BATTERIES

Panuwat Watthaisong

A Thesis Submitted in Partial Fulfillment of the Requirements for the

Degree of Master of Science in Chemistry

Suranaree University of Technology

Academic Year 2020

การศึกษากลไกการสลายตัวของเอทิลีนคาร์บอเนตบนขั้วแอโนดที่เป็นคาร์บอนในโซเดียมไอออนแบตเตอรี

นายภาณุวัฒน์ วัดไธสง

วิทยานิพนธ์นี้เป็นส่วนหนึ่งของการศึกษาตามหลักสูตรปริญญาวิทยาศาสตรมหาบัณฑิต
สาขาวิชาเคมี
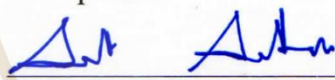มหาวิทยาลัยเทคโนโลยีสุรนารี
ปีการศึกษา 2563

MECHANISTIC STUDY OF ETHYLENE CARBONATE

DECOMPOSITION ON CARBON ANODE OF SODIUM-ION

BATTERIES

Suranaree University of Technology has approved this thesis submitted in partial fulfillment of the requirements for a Master's Degree.

Thesis Examining Committee

_____
(Prof. Dr. James R. Ketudat-Cairns)

Chairperson

_____
(Asst. Prof. Dr. Suwit Suthirakun)

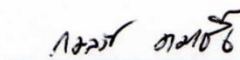Member (Thesis Advisor)

_____
(Dr. Pussana Hirunsit)
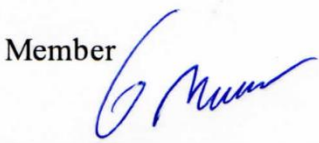
Member (Thesis Co-Advisor)
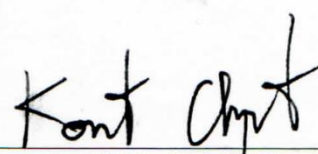
_____
(Prof. Dr. Kritsana Sagarik)

Member

_____
(Dr. Kamonwad Ngamchuea)

Member

_____   _____
(Assoc. Prof. Flt. Lt. Dr. Kontorn Chamniprasart)   (Assoc. Prof. Dr. Worawat Meevasana)

Vice Rector for Academic Affairs   Dean of Institute of Science

and Internationalization

ภาณุวัฒน์ วัดไธสง : การศึกษากลไกการสลายตัวของเอทิลีนคาร์บอเนตบนขั้วแอโนดที่
เป็นคาร์บอนในโซเดียมไอออนแบตเตอรี (MECHANISTIC STUDY OF ETHYLENE
CARBONATE DECOMPOSITION ON CARBON ANODE OF SODIUM-ION
BATTERIES) อาจารย์ที่ปรึกษา : ผู้ช่วยศาสตราจารย์ ดร.สุวิทย์ สุธีรากุล, 87 หน้า.

วิทยานิพนธ์นี้ได้ใช้การคำนวณแบบเฟิร์สทพรินซิเพิลโดยวิธี DFT ในการศึกษากลไกการ
สลายตัวของเอทิลีนคาร์บอเนตซึ่งเป็นอิเล็กโทรไลต์ที่ได้รับความนิยมอย่างแพร่หลายสำหรับ
โซเดียมไอออนแบตเตอรี โดยจะทำการศึกษาบนพื้นผิวของวัสดุประเภทคาร์บอน และมีการศึกษา
ผลของหมู่ฟังก์ชันของวัสดุต่อกลไกการสลายตัว ผลการคำนวณแสดงให้เห็นว่า การมีหมู่ฟังก์ชัน
อีพ็อกซีบนพื้นผิวของวัสดุคาร์บอนจะส่งผลกระทบที่ชัดเจนต่อการสลายตัวของเอทิลีนคาร์บอเนต
ซึ่งผลกระทบดังกล่าวจะมีความแตกต่างกันไปในแต่ละระบบที่ทำการศึกษา โดยหากทำการศึกษา
ในระบบที่มีโซเดียมในระบบเพียงหนึ่งอะตอม จะได้ผลลัพธ์ว่าการที่มีหมู่อีพ็อกซีจะทำให้การ
สลายตัวของเอทิลีนคาร์บอเนตในทุก ๆ เส้นทางของปฏิกิริยาเกิดได้ช้าลง แต่ถ้าหากจำนวนโซเดียม
มีสองอะตอมในระบบ แนวโน้มการสลายตัวของเอทิลีนคาร์บอเนตจะมีการเปลี่ยนแปลงไป และถ้า
หากทำการศึกษาผลของโมเลกุลอิเล็กโทรไลต์ที่ล้อมรอบโมเลกุลที่มีการสลายตัวจะพบว่าผลที่ได้
ตรงกันข้าม โดยการมีอยู่ของหมู่ฟังก์ชันอีพ็อกซีในกรณีนี้จะทำหน้าที่ในการเร่งปฏิกิริยาการสลายตัว
ให้เกิดได้ง่ายขึ้น

สาขาวิชาเคมี   ลายมือชื่อนักศึกษา_____

ปีการศึกษา 2563   ลายมือชื่ออาจารย์ที่ปรึกษา_____

               ลายมือชื่ออาจารย์ที่ปรึกษาร่วม_____

PANUWAT WATTHAISONG : MECHANISTIC STUDY OF ETHYLENE CARBONATE DECOMPOSITION ON CARBON ANODE OF SODIUM-ION BATTERIES. THESIS ADVISOR : ASST.PROF. SUWIT SUTHIRAKUN, Ph.D. 87 PP.

SOLID ELECTROLYTE INTERPHASE/SODIUM-ION BATTERY/EPOXY GROUP/ DENSITY FUNCTIONAL THEORY/ /ELECTROLYTE DECOMPOSITION

In this thesis, we utilized first-principles calculations based on DFT method to study the decomposition mechanisms of ethylene carbonate (EC) which is one of the most common electrolytes used in sodium-ion batteries (SIBs). Our calculations were performed on carbon-based anode material with and without the presence of epoxy group in order to evaluate its role. Computations reveal that epoxy group has a significant role on decomposition mechanisms of EC depending on the their local environment. With only one Na atom on the surface, the presence of epoxy group decreases the amount of EC decomposition due to an increase of reaction energies and reaction barriers. If we introduce one more Na atom onto the surface, the trend of energy for EC decomposition mechanism is changed. Furthermore, the effect of solvent environment was evaluated by adding four more EC molecules on the surfaces. In this case, the presence of epoxy group facilitates the EC decomposition through chemical interaction and might cause the formation of thicker solid-electrolyte interphase than that without epoxy group.

School of Chemistry

Academic Year 2020

Student's Signature_____

Advisor's Signature_____

Co-Advisor's Signature_____

ACKNOWLEDGEMENTS

CONTENTS

CONTENTS (Continued)

CONTENTS (Continued)

LIST OF TABLES

LIST OF FIGURES

LIST OF FIGURES (Continued)

LIST OF FIGURES (Continued)

LIST OF FIGURES (Continued)

LIST OF ABBREVIATIONS

LIBs   = Lithium-ion Batteries

SIBs   = Sodium-ion Batteries

SEI   = Solid Electrolyte Interphase

EC   = Ethylene Carbonate

DFT   = Density Functional Theory

VASP   = Vienna Ab Initio Simulation Package

GGA   = Generalized Gradient Approximation

LDA   = Local Density Approximation

LSDA   = Local Spin Density Approximation

PAW   = Projector-Augmented Wave

PBE   = Perdew-Burke-Ernzerhof

CI-NEB   = Climbing Image-Nudged Elastic Band

MEP   = Minimum Energy Path

TS   = Transition State

HOMO   = Highest Occupied Molecular Orbital

LUMO   = Lowest Unoccupied Molecular Orbital

CHAPTER I

INTRODUCTION

1.1   Background and significance

During the past few years, the increasing need for sustainable energy sources has been substantially driven the demand of energy storages, especially lithium-ion batteries (LIBs). Although LIBs have high energy density and good electrochemical properties, they still encounter challenging questions regarding safety, lifetime, and poor low-temperature performance. In particular, the cost of Li is quite high due to an uneven distribution of Li sources among a few companies worldwide (Grosjean *et al.*, 2012; Tarascon and Armand, 2001; Yoo *et al.*, 2013). Sodium-ion batteries (SIBs) are promising to be an alternative replacement of LIBs because sodium is the second lightest and smallest alkali metal where its resources are more abundant and widely distributed (Ober, 2018; Vaalma *et al.*, 2018). Since chemical properties of sodium are similar to that of lithium, SIBs share a similar rocking-chair operation mechanism with LIBs, which potentially provide high reversibility and long cycling life (Figure 1.1) (Bommier *et al.*, 2016; Huang *et al.*, 2018; Nayak *et al.*, 2018b; Yabuuchi *et al.*, 2014). However, there remain several challenges, including designing and fabricating suitable electrodes, developing advanced electrolytes, and optimizing the electrode-electrolyte interphase to enhance SIBs performance and lifetime that can reach the current stage of LIBs technology.

During the charge process, mainly in the first charge, a solid electrolyte interphase (SEI) layer forms by the reduction of organic solvents in the electrolyte at the anode of SIBs. Recent computational studies indicate that sodium ion is likely to be solvated by ethylene carbonate (EC) over propylene carbonate and other electrolyte molecules, due to its high dielectric constant (Kamath *et al.*, 2014; Shakourian-Fard *et al.*, 2015). Thus, various electrolyte decomposition studies were devoted for EC decomposition mechanisms (Figure 1.2). It is accepted that the SEI layer has a profound effect to the performance of the batteries, including an impact on its initial capacity loss, self-discharge characteristics, cycle life, rate capability, and safety (An *et al.*, 2016; Bommier *et al.*, 2016; Horstmann *et al.*, 2019). On one hand, the formation of the SEI intrinsically consumes the anode and electrolyte, leading to a low efficiency. On the other hand, the SEI effectively prevents further decomposition of the electrolyte. The SEI layer is considered as the least understood and most subtle component of the metal-ion battery systems (Peled, 1979a; Peled *et al.*, 1995a; Peled *et al.*, 1995b; Peled and Menkin, 2017). Therefore, a good understanding of the SEI formation is very critical for the development of SIBs.

Owing to the fact that formation of the SEI layer usually occurs at the anode of the batteries, the properties for SEI strongly depend on the sodiation/desodiation characteristics of each anode material. Identifying a suitable anode material is one major issue for the development of SIBs because sodiation is thermodynamically unfavorable in graphite, which is the standard anode for LIBs (Jache and Adelhelm, 2014). Carbon-based materials hold the most promise considering the various sources of precursors and cost. As a result, many carbon-based materials, such as hard carbons (Bommier *et al.*, 2014; Ding *et al.*, 2013; Hasegawa *et al.*, 2015), heteroatom-doped

carbons (Li *et al.*, 2019; Xu *et al.*, 2015; Zhang *et al.*, 2016), reduced graphene oxide (Liu *et al.*, 2018; Zhao *et al.*, 2019), carbon nanotubes (Chen *et al.*, 2016; Gu *et al.*, 2016; Que *et al.*, 2018), and graphene-related materials (Chen *et al.*, 2016; Gu *et al.*, 2016; Que *et al.*, 2018) have been proposed as the anode of SIBs.
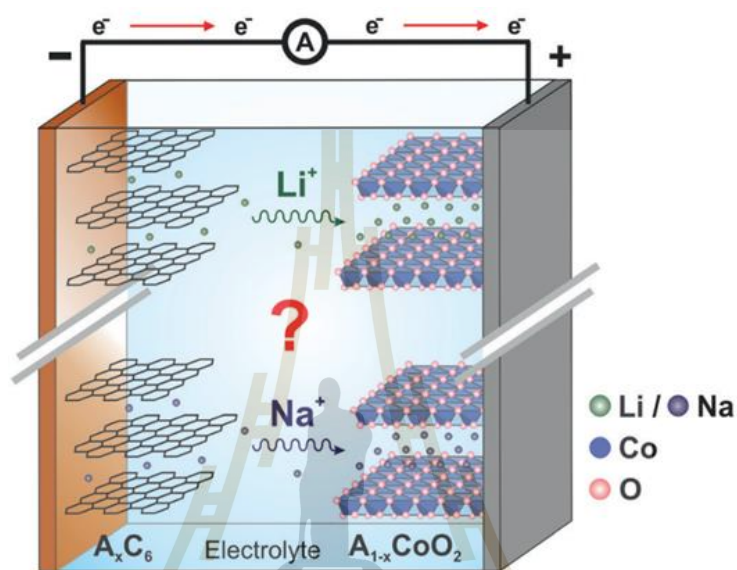
Figure 1.1 Schematic comparison between SIBs and LIBs. SIBs can operate the same way as LIBs with sodium ions intercalating into two host structures, but the increase in ion size leads to significant changes in the cell behavior (Nayak *et al.*, 2018a).

As previously reported, production of synthetic porous carbon via carbonization of carbonaceous species leads to significant incorporation of oxygen-containing functional groups on the surface of the resulting carbon materials (Emmerich, 1995; Gilbert *et al.*, 1962; Kipling *et al.*, 1964). It is believed that epoxy and hydroxyl groups prefer to be located on the basal plane, while carbonyl, ester and carboxylic groups are found at the sheet edges, as shown in Figure 1.3 (Compton *et al.*, 2010; Stankovich *et al.*, 2007; Stankovich *et al.*, 2006). It has been revealed that these O-functionalization

are beneficial to improve the electrochemical performance of the carbon-based anodes due to the enhanced reactivity and electronic conductivity (Shao *et al.*, 2013). Furthermore, these oxygen-containing functional groups could participate in the SEI formation reactions, resulting in different compositions and morphologies of the SEI layer.
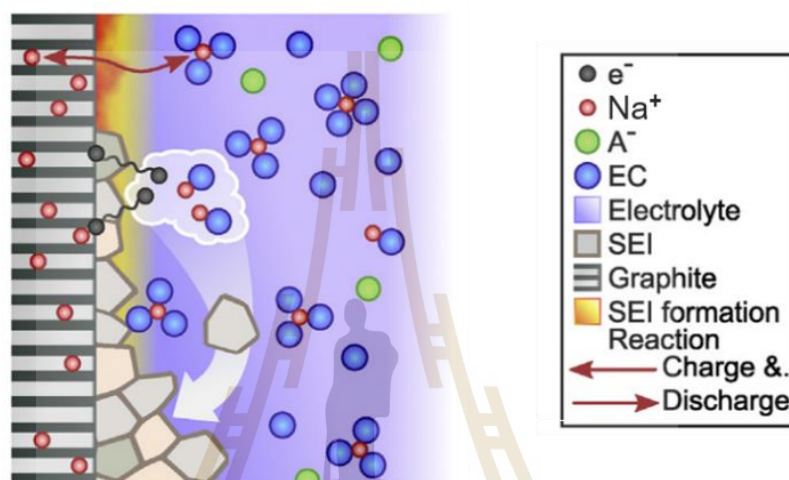
Figure 1.2 Cross-section through the negative electrode, the SEI, and the electrolyte. Solvent, sodium ions, and electrons are mobile species and move as indicated by the corresponding arrows. Initial SEI formation: electrons tunnel, electrolyte is reduced, and reduction products precipitate as solid film (Horstmann *et al.*, 2019).
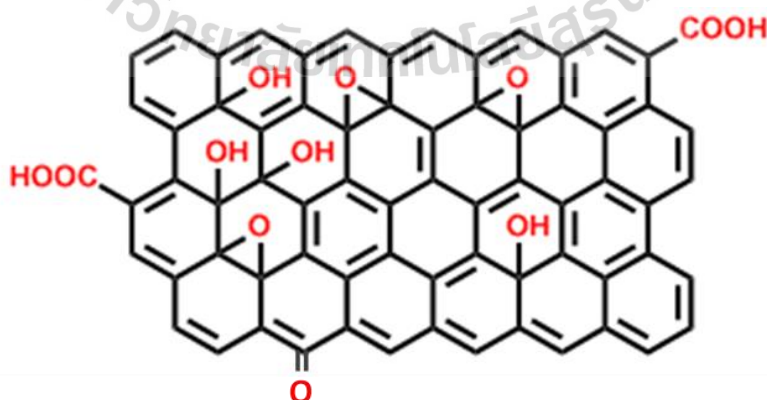
Figure 1.3 Oxygen-containing groups decorate surface of carbon materials, including epoxide, hydroxyl, carbonyl, and carboxyl group (Carneiro *et al.*, 2019).

1.2   Literature review

A critical component of rechargeable alkali metal-ion batteries is the passivation layer that forms on the carbon anode during the first cycle, namely SEI. Peled was the first author to introduce the concept of SEI and its fundamental physicochemical properties in 1979 (Peled, 1979b). The SEI is built up mostly from decomposition of electrolyte components. In terms of properties, this SEI layer should be electronically insulating, in order to prevent continual electrolyte decomposition and SEI growth, as well as ionically conductive, to enable efficient cation shuttling through it. Formation of a stable and thin layer is essential for a long-lasting battery capable of high-power applications. Goodenough's model elucidated how the SEI works in LIBs from the energy band aspect (Figure 1.4) (Goodenough and Kim, 2010). When the lowest unoccupied molecular orbital (LUMO) of the electrolyte is higher than the Fermi energy of anode, the electrolyte is stable in the battery; otherwise, the electrolyte can be reduced. Similarly, if the cathode has a μ_c (cathode Fermi energy) that is below the highest occupied molecular orbital (HOMO), a passivation layer will be required to block electron transfer from electrolyte HOMO to the cathode. The energy separation between the anode and cathode needs to be as high as possible to increase the energy density of the redox pair. Therefore, electrode and electrolyte composition are two main factors that determine the properties of the SEI. In addition, similar energy storage mechanism in LIBs and SIBs enables us to understand and design new electrode materials for SIBs based on experience gained from LIBs.

In term of electrode, the graphite anode reached major commercial success partly for LIBs because of the high quality SEI formation that is capable of sustaining thousands of charging and discharging cycles (Raccichini *et al.*, 2015). However, the

large sodium ion radius (1.02 Å) results in the sluggish reaction kinetics and difficult intercalation/de-intercalation behavior in the commercial graphite anodes during charge/discharge process. Thus, A variety of options have been explored, including carbon materials (Adams *et al.*, 2019; Hou *et al.*, 2017; Komaba *et al.*, 2011; Liu and Li, 2018; Zhong *et al.*, 2018), phosphorous (Li and Zhao, 2018; Xia *et al.*, 2017), organic compounds (Park *et al.*, 2012), metal oxides (Fang *et al.*, 2020; Jiang *et al.*, 2014), sodium ternary compounds (Muñoz-Márquez *et al.*, 2017), and various types of alloys (Kim *et al.*, 2014; Song *et al.*, 2019). Among these candidates,
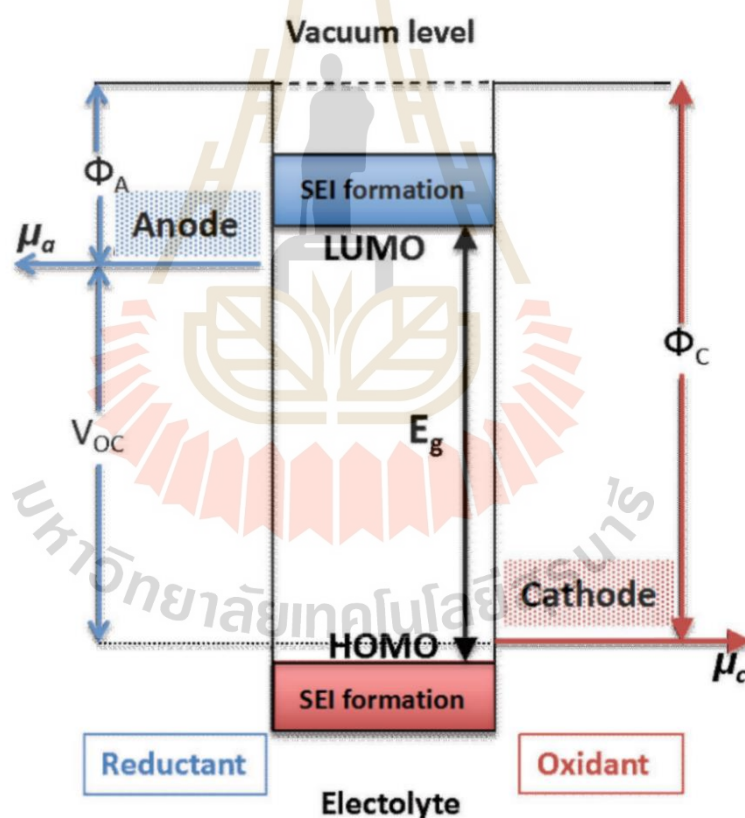
Figure 1.4 Schematic of an energy diagram of a nonaqueous SIBs system. Φ_A and Φ_C are anode and cathode work functions. E_g is the band gap that corresponds to the thermodynamically stable window of the electrolyte. When $\mu_a >$ LUMO and/or $\mu_c <$ HOMO, an SEI layer will be formed (Yu *et al.*, 2018).

carbon-based materials are one of the most widely explored categories of materials. Due to the unique combination of chemical and physical properties such as cost effectiveness, high abundance, excellent corrosion resistance, moderate conductivity and relatively high surface area (Adams *et al.*, 2019; Zhong *et al.*, 2018).

In contrast to LIBs, there have been limited fundamental explorations on the formation of the SEI layer on carbon-based anode in SIBs (Bommier *et al.*, 2016; Komaba *et al.*, 2011). It has been reported that the SEI films on the hard carbon electrode consist of both organics (R-COCO$_2$Na, R-COONa, R-ONa or polymeric species) in the exterior and inorganics (Na$_2$CO$_3$, NaF or NaCl) in the interior, with increased inorganic composition as compared to SEI in LIBs (Pan *et al.*, 2017). XPS results confirm that in the Na-ion case a surface film is formed on the hard carbon surface with a minimum thickness of 5–10 nm, corresponding to the XPS penetration depth (Komaba *et al.*, 2011). Moreover, it was found that continuous formation of the SEI is the main reason for capacity fading, rather than degeneration of the HC materials and cause serious kinetic problems (Bommier *et al.*, 2016). More efforts should be carried out to construct durable interfaces to achieve high-performance HC electrodes. Due to SEI formation occurrence via electrolyte decomposition, the optimal electrolyte will form a suitable SEI layer on the anode and improve cycling and rate performance of the cells. A general list of properties required for liquid electrolytes in SIBs are similar to those required for LIBs: (i) chemically stable, (ii) electrochemically stable, (iii) thermally stable, (iv) ionically conductive and electronically insulating and (v) low toxicity with low production cost (Aurbach *et al.*, 2004; Xu, 2014). The majority of electrolytes used for SIBs rely on sodium salts of NaClO$_4$, NaPF$_6$, or Na bis(trifluoromethane)-sulfonimide, dissolved in a carbonate-based organic solvent.

EC is an indispensable organic solvent component of non-aqueous liquid electrolytes for SIBs due to high dielectric constant and its stability at the anode surface (Payne and Theodorou, 1972; Ponrouch *et al.*, 2012; Song *et al.*, 1999), which is crucial for dissociating sodium salts in solution. Based on these properties, a numerous number of studies have focused on EC decomposition mechanism.

The formation mechanism of SEI is quite complex and influenced by various factors. Only the experimental studies are not enough to directly capture the reactions at the electrode/electrolyte interface and separately evaluate the role of each factor. Theoretical studies based on DFT are powerful tool for examining behavior of this formation mechanism on the atomic scale. Prior to the success of LIBs, most theoretical studies for SEI formation mechanism have primarily focused on LIBs system (Choi *et al.*, 2019; Ganesh *et al.*, 2012; Leung, 2013; Leung and Budzien, 2010; Leung *et al.*, 2011; Mutoh *et al.*, 2016; Ohba *et al.*, 2019; Takenaka *et al.*, 2014; Vollmer *et al.*, 2004; Wang *et al.*, 2018; Wang *et al.*, 2020; Wang *et al.*, 2002; Wang *et al.*, 2001) and very limited number of computational studies addressing for SIBs (Kumar *et al.*, 2016; Liu *et al.*, 2017; Purushotham *et al.*, 2016; Soto *et al.*, 2017; Takenaka *et al.*, 2015). Nevertheless, the experiences and knowledge from the investigations on LIBs can help model and understand the formation mechanism of SEI on SIBs. Numerous electrolyte decomposition studies were devoted for EC decomposition mechanisms due to the highest reduction potential and the Li- and Na-ion were usually solvated by EC molecules as the first solvation shell (Kamath *et al.*, 2014; Xu, 2004). In 2000, Li and Balbuena (Li and Balbuena, 2000) first applied quantum chemical calculations to investigate the EC reduction mechanism that experimentally proposed by Aurbach *et al* (Aurbach *et al.*, 1997). The calculated results suggest that even when the electron

affinity of EC in gas phase is negative, they are stabilized when becoming open-ring anions. A sequential two-electron transfer mechanism applied to EC is thermodynamically feasible. The rate-determining step is identified as the ring-opening of the solvent molecule occurred by a nucleophilic attack in the first electron-transfer reaction. Then, the second electron transfer takes place to break the second bond of the solvent ring at a much faster rate. The main product of two electron reduction reaction of EC was found to be $LiCO_3^-$ anions that can further attack another solvent molecule to form lithium ethylene dicarbonate or paired by another lithium ion, precipitating as insoluble Li_2CO_3 (Li and Balbuena, 2000). Other computational works have extensively studied the decomposition mechanisms of EC in LIBs where two different two-electron decomposition routes have been proposed as schematically shown in Figure 1.5 (Leung, 2013; Leung and Budzien, 2010; Ma and Balbuena, 2014; Martinez de la Hoz *et al.*, 2013; Okuno *et al.*, 2019; Østergaard *et al.*, 2018; Qin *et al.*, 2019; Takenaka and Nagaoka, 2019). The first route is a reduction of EC to C_2H_4 gas and a CO_3^{2-} ion via cleavage of $C_E\mathrm{-}O_E$ bonds (Figure 1.5(b)). The second route is a reduction via $C_C\mathrm{-}O_E$ bonds of EC forms CO gas and a $C_2H_4O_2^{2-}$ ion (Figure 1.5(d)). The first route normally occurs when electron transfer is fast while the second occurs via slower electron transfer rate.

From experimental works, different type, morphology, and defect of electrode significantly affect the SEI formation mechanism and the SEI layer (An *et al.*, 2016; Gauthier *et al.*, 2015; Verma *et al.*, 2010). Thus, the computational calculations of EC decomposition reaction on several explicit electrode surface have been performed to simulate the reaction at electrode/electrolyte interface. On graphite anode, graphite edge region strongly affects EC decomposition reaction and different results were found

for different termination (Ganesh *et al.*, 2012; Leung and Budzien, 2010). The calculations were performed with the LiC_6 structure which is fully-lithiated graphite. In reactions occurring at electrode surfaces, electron most likely flow directly to the decomposing EC molecules coordinated to surface Li's without becoming first delocalized in the liquid. As such, this mechanism should not strongly depend on the EC liquid density or the simulation cell size. C=O and C−OH edges give strong driving forces and support the through both routes. In contrast, a H-terminated surface does not reduce EC (Ganesh *et al.*, 2012). Moreover, the reductive decomposition reaction of EC was found to occurs before the intercalation of the lithium ions into graphite (Ohba *et al.*, 2019).

The solvation effect on EC decomposition was examined by Wang *et al.* (Wang *et al.*, 2001). They found that the coordination of EC with Li^+ enhances the reduction of EC. Increasing number of EC molecules decreases the energy barrier for EC reduction. This difference could be explained by the electronic structure of EC^-. In gas-phase calculation, the excess electron lies outside the molecule and does not occupy C_E–O_E antibonding orbital which is not facilitate the bond-breaking. In liquid EC, the excess electron is initially delocalized within one or more EC molecules. When the geometries of the EC solution change until it is proper for the electron to localize on one EC and substantially populates orbitals on C and O atoms, bond-breaking pathways with rates different from that in the gas phase emerge. In contrary, the different result was found for EC decomposition on Ca anode (Young and Smeu, 2018a). In this work, the effect of surrounding EC molecules slows electron transfer and causes the CO route to dominate. The calculated results indicated that the solvation effect plays an important role in determining mechanism of EC decomposition.

CO₃²⁻ route

$$EC + 2e^- \rightarrow CO_3^{2-} + C_2H_4$$

CO route

$$EC + e^- \rightarrow o\text{-}EC^- + e^- \rightarrow C_2H_4O_2^{2-} + CO$$
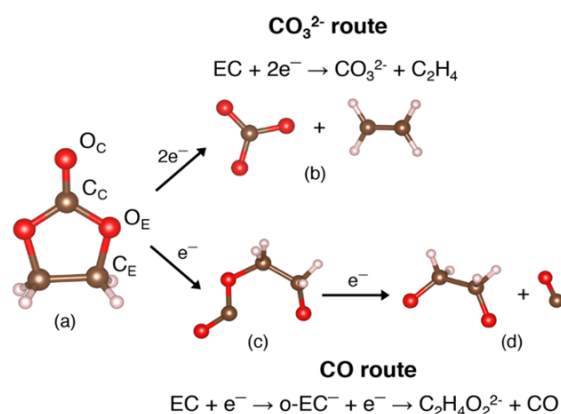
Figure 1.5 An (a) ethylene carbonate molecule (with the ethylene and carbonate C and O atoms indicated by E and C, respectively) can decompose into (b) a combination of a CO_3^{2-} ion and a C_2H_4 molecule, or into (c) a ring-opened chain followed by (d) a combination of a $C_2H_4O_2^{2-}$ ion and a CO molecule (Young and Smeu, 2018b).

For SIBs, Shenoy *et al*. carried out DFT calculations to investigate the fundamental mechanisms of decomposition of electrolyte solvents including EC, vinylene carbonate , and fluoroethylene carbonate in the vicinity of a Na ion (Kumar *et al.*, 2016). Their computations indicate that EC is the main cause for the continuous growth of SEI observed in SIBs due to its high reduction potential and low barrier for the ring opening. The vinylene carbonate and fluoroethylene carbonate additive molecules were found to protect solvent molecules from reductive decomposition. Also, they can change the decomposition pathways leading to qualitatively different and potentially stable SEI products. Liu *et al.* also investigate the decomposition mechanism of EC in a quite similar way. They conclude that of EC, propylene carbonate, and vinylene carbonate decomposition could produce $(CH_2CH_2CO_3Na)_2$, which is one of the organic SEI components. In addition, the product of Na_2CO_3 could

be formed on anode surface through two-electron reduction of EC (Liu *et al.*, 2017). For the DFT calculations of electrolyte decomposition in hard carbon, the EC molecules intercalate between carbon layer and undergo ring opening at the graphite edge, whereas decomposed dimethyl carbonate molecules are observed to attach to the graphite edge (Soto *et al.*, 2017). The result is different from LIB system that the EC bonds get reduced on unsaturated carbon edges without intercalation between the carbon layer.

Based on the experimental and computational works cited above, the role of oxygen functional group of carbon-based anodes on EC decomposition mechanism are still unclear. In this work, we carried out DFT calculations to obtain theoretical insight into the decomposition mechanisms of EC electrolyte on carbon anode. This is the molecular initial step of the SEI formation on SIB anode that plays an important role in determining the performance of the battery. The role of oxygen-containing group presence on carbon anode is investigated. We analyzed electronic charges and energy profiles of EC decomposition mechanisms on graphene surfaces both with and without an epoxy group presence. The influence of the surrounding electrolyte molecules on the EC decomposition energetic profile is also investigated by explicitly increasing number of EC molecules surrounding the Na ion. The understanding of solvent decomposition pathways would enable us to gain the insight of SEI formation mechanisms at very early stage of charge process of the battery.

1.3   References

Adams, R. A., Varma, A., and Pol, V. G. (2019). Carbon Anodes for Nonaqueous Alkali Metal-Ion Batteries and Their Thermal Safety Aspects. **Adv. Energy Mater.** 9: 1900550.

An, S. J., Li, J., Daniel, C., Mohanty, D., Nagpure, S., and Wood, D. L. (2016). The State of Understanding of The Lithium-Ion-Battery Graphite Solid Electrolyte Interphase (SEI) and Its Relationship to Formation Cycling. **Carbon**. 105: 52.

Aurbach, D., Levi, M. D., Levi, E., and Schechter, A. (1997). Failure and Stabilization Mechanisms of Graphite Electrodes. **J. Phys. Chem. B**. 101: 2195.

Aurbach, D., Talyosef, Y., Markovsky, B., Markevich, E., Zinigrad, E., Asraf, L., Gnanaraj, J. S., and Kim, H.-J. (2004). Design of Electrolyte Solutions for Li and Li-ion Batteries: A Review. **Electrochim. Acta**. 50: 247.

Bommier, C., Luo, W., Gao, W.-Y., Greaney, A., Ma, S., and Ji, X. (2014). Predicting Capacity of Hard Carbon Anodes in Sodium-Ion Batteries Using Porosity Measurements. **Carbon**. 76: 165.

Bommier, C., Leonard, D., Jian, Z., Stickle, W. F., Greaney, P. A., and Ji, X. (2016). New Paradigms on the Nature of Solid Electrolyte Interphase Formation and Capacity Fading of Hard Carbon Anodes in Na-Ion Batteries. **Adv. Mater. Interfaces**. 3: 1600449.

Carneiro, P., Morais, S., and Pereira, M. C. (2019). Nanomaterials towards Biosensing of Alzheimer's Disease Biomarkers. **Nanomaterials (Basel, Switzerland)**. 9: 1663.

Chen, H.-Y., Bucher, N., Hartung, S., Li, L., Friedl, J., Liou, H.-P., Sun, C.-L., Stimming, U., and Srinivasan, M. (2016). A Multi-Walled Carbon Nanotube

Core with Graphene Oxide Nanoribbon Shell as Anode Material for Sodium Ion Batteries. **Adv. Mater. Interfaces**. 3: 1600357.

Choi, W. I., Park, M. S., Shim, Y., Kim, D. Y., Kang, Y.-S., Lee, H. S., and Koh, M. (2019). Reductive Reactions via Excess Li in Mixture Electrolytes of Li ion Batteries: An Ab Initio Molecular Dynamics Study. **Phys. Chem. Chem. Phys.** 21: 5489.

Compton, O. C., Dikin, D. A., Putz, K. W., Brinson, L. C., and Nguyen, S. T. (2010). Electrically Conductive "Alkylated" Graphene Paper via Chemical Reduction of Amine-Functionalized Graphene Oxide Paper. **Adv. Mater.** 22: 892.

Ding, J., Wang, H., Li, Z., Kohandehghan, A., Cui, K., Xu, Z., Zahiri, B., Tan, X., Lotfabad, E. M., Olsen, B. C., and Mitlin, D. (2013). Carbon Nanosheet Frameworks Derived from Peat Moss as High Performance Sodium Ion Battery Anodes. **ACS Nano**. 7: 11004.

Emmerich, F. G. (1995). Evolution with Heat Treatment of Crystallinity in Carbons. **Carbon**. 33: 1709.

Fang, S., Bresser, D., and Passerini, S. (2020). Transition Metal Oxide Anodes for Electrochemical Energy Storage in Lithium- and Sodium-Ion Batteries. **Adv. Energy Mater.** 10: 1902485.

Ganesh, P., Kent, P. R. C., and Jiang, D.-e. (2012). Solid–Electrolyte Interphase Formation and Electrolyte Reduction at Li-Ion Battery Graphite Anodes: Insights from First-Principles Molecular Dynamics. **J. Phys. Chem. C**. 116: 24476.

Gauthier, M., Carney, T. J., Grimaud, A., Giordano, L., Pour, N., Chang, H. H., Fenning, D. P., Lux, S. F., Paschos, O., Bauer, C., Maglia, F., Lupart, S., Lamp,

P., and Shao-Horn, Y. (2015). Electrode-electrolyte Interface in Li-ion Batteries: Current Understanding and New Insights. **J. Phys. Chem. Lett.** 6: 4653.

Gilbert, J. B., Kipling, J. J., McEnaney, B., and Sherwood, J. N. (1962). Carbonization of polymers I—Thermogravimetric analysis. **Polymer**. 3: 1.

Goodenough, J. B., and Kim, Y. (2010). Challenges for Rechargeable Li Batteries. **Chem. Mater.** 22: 587.

Grosjean, C., Miranda, P. H., Perrin, M., and Poggi, P. (2012). Assessment of world lithium resources and consequences of their geographic distribution on the expected development of the electric vehicle industry. **Renew. Sust. Energ. Rev.** 16: 1735.

Gu, T., Zhou, M., Liu, M., Wang, K., Cheng, S., and Jiang, K. (2016). A polyimide–MWCNTs composite as high performance anode for aqueous Na-ion batteries. **RSC Adv.** 6: 53319.

Hasegawa, G., Kanamori, K., Kannari, N., Ozaki, J.-i., Nakanishi, K., and Abe, T. (2015). Hard Carbon Anodes for Na-Ion Batteries: Toward a Practical Use. **ChemElectroChem**. 2: 1917.

Horstmann, B., Single, F., and Latz, A. (2019). Review on multi-scale models of solid-electrolyte interphase formation. **Curr. Opin. Electrochem.** 13: 61.

Hou, H., Qiu, X., Wei, W., Zhang, Y., and Ji, X. (2017). Carbon Anode Materials for Advanced Sodium-Ion Batteries. **Adv. Energy Mater.** 7: 1602898.

Huang, Y., Zheng, Y., Li, X., Adams, F., Luo, W., Huang, Y., and Hu, L. (2018). Electrode Materials of Sodium-Ion Batteries toward Practical Application. **ACS Energy Lett**. 3: 1604.

Jache, B., and Adelhelm, P. (2014). Use of Graphite as a Highly Reversible Electrode with Superior Cycle Life for Sodium-Ion Batteries by Making Use of Co-Intercalation Phenomena. **Angew. Chem. Int. Ed.** 53: 10169.

Jiang, Y., Hu, M., Zhang, D., Yuan, T., Sun, W., Xu, B., and Yan, M. (2014). Transition metal oxides for high performance sodium ion battery anodes. **Nano Energy**. 5: 60.

Kamath, G., Cutler, R. W., Deshmukh, S. A., Shakourian-Fard, M., Parrish, R., Huether, J., Butt, D. P., Xiong, H., and Sankaranarayanan, S. K. R. S. (2014). In Silico Based Rank-Order Determination and Experiments on Nonaqueous Electrolytes for Sodium Ion Battery Applications. **J. Phys. Chem. C**. 118: 13406.

Kim, Y., Ha, K. H., Oh, S. M., and Lee, K. T. (2014). High-capacity anode materials for sodium-ion batteries. **Chemistry**. 20: 11980.

Kipling, J. J., Sherwood, J. N., Shooter, P. V., and Thompson, N. R. (1964). Factors influencing the graphitization of polymer carbons. **Carbon**. 1: 315.

Komaba, S., Murata, W., Ishikawa, T., Yabuuchi, N., Ozeki, T., Nakayama, T., Ogata, A., Gotoh, K., and Fujiwara, K. (2011). Electrochemical Na Insertion and Solid Electrolyte Interphase for Hard-Carbon Electrodes and Application to Na-Ion Batteries. **Adv. Funct. Mater.** 21: 3859.

Kumar, H., Detsi, E., Abraham, D. P., and Shenoy, V. B. (2016). Fundamental Mechanisms of Solvent Decomposition Involved in Solid-Electrolyte Interphase Formation in Sodium Ion Batteries. **Chem. Mater.** 28: 8930.

Leung, K., and Budzien, J. L. (2010). Ab initio molecular dynamics simulations of the initial stages of solid–electrolyte interphase formation on lithium ion battery graphitic anodes. **Phys. Chem. Chem. Phys.** 12: 6583.

Leung, K., Qi, Y., Zavadil, K. R., Jung, Y. S., Dillon, A. C., Cavanagh, A. S., Lee, S.-H., and George, S. M. (2011). Using Atomic Layer Deposition to Hinder Solvent Decomposition in Lithium Ion Batteries: First-Principles Modeling and Experimental Studies. **J. Am. Chem. Soc.** 133: 14741.

Leung, K. (2013). Two-electron reduction of ethylene carbonate: A quantum chemistry re-examination of mechanisms. **Chem. Phys. Lett.** 568-569: 1.

Li, C., Li, J., Zhang, Y., Cui, X., Lei, H., and Li, G. (2019). Heteroatom-doped hierarchically porous carbons derived from cucumber stem as high-performance anodes for sodium-ion batteries. **J. Mater. Sci.** 54: 5641.

Li, T., and Balbuena, P. B. (2000). Theoretical studies of the reduction of ethylene carbonate. **Chem. Phys. Lett.** 317: 421.

Li, Z., and Zhao, H. (2018). Recent developments of phosphorus-based anodes for sodium ion batteries. **J. Mater. Chem. A**. 6: 24013.

Liu, Q., Mu, D., Wu, B., Wang, L., Gai, L., and Wu, F. (2017). Density Functional Theory Research into the Reduction Mechanism for the Solvent/Additive in a Sodium-Ion Battery. **ChemSusChem**. 10: 786.

Liu, T., and Li, X. (2018). Biomass-derived nanostructured porous carbons for sodium ion batteries: a review. **Mater. Tech.** 34: 232.

Liu, Y., Zhang, A., Shen, C., Liu, Q., Cai, J., Cao, X., and Zhou, C. (2018). Single-step flash-heat synthesis of red phosphorus/graphene flame-retardant composite as flexible anodes for sodium-ion batteries. **Nano Res.** 11: 3780.

Ma, Y., and Balbuena, P. B. (2014). DFT Study of Reduction Mechanisms of Ethylene Carbonate and Fluoroethylene Carbonate on Li$^+$-Adsorbed Si Clusters. **J. Electrochem. Soc.** 161: E3097.

Martinez de la Hoz, J. M., Leung, K., and Balbuena, P. B. (2013). Reduction Mechanisms of Ethylene Carbonate on Si Anodes of Lithium-Ion Batteries: Effects of Degree of Lithiation and Nature of Exposed Surface. **ACS Appl. Mater. Interfaces**. 5: 13457.

Muñoz-Márquez, M. Á., Saurel, D., Gómez-Cámer, J. L., Casas-Cabanas, M., Castillo-Martínez, E., and Rojo, T. (2017). Na-Ion Batteries for Large Scale Applications: A Review on Anode Materials and Solid Electrolyte Interphase Formation. **Adv. Energy Mater.** 7: 1700463.

Mutoh, M., Abe, S., Kusaka, T., Nakamura, M., Yoshida, Y., Iida, J., and Tachikawa, H. (2016). Density Functional Theory (DFT) Study on the Ternary Interaction System of the Fluorinated Ethylene Carbonate, Li$^+$ and Graphene Model. **Atoms**. 4: 4.

Nayak, P. K., Yang, L., Brehm, W., and Adelhelm, P. (2018a). From Lithium-Ion to Sodium-Ion Batteries: Advantages, Challenges, and Surprises. **Angew. Chem. Int. Ed. Engl.** 57: 102.

Nayak, P. K., Yang, L., Brehm, W., and Adelhelm, P. (2018b). From Lithium-Ion to Sodium-Ion Batteries: Advantages, Challenges, and Surprises. **Angew. Chem. Int. Ed.** 57: 102.

Ober, J. A. (2018). Mineral commodity summaries 2018. Reston, VA, U.S.G. Survey, 204.

Ohba, N., Ogata, S., and Asahi, R. (2019). Hybrid Quantum-Classical Simulation of Li Ion Dynamics and the Decomposition Reaction of Electrolyte Liquid at a Negative-Electrode/Electrolyte Interface. **J. Phys. Chem. C**. 123: 9673.

Okuno, Y., Ushirogata, K., Sodeyama, K., Shukri, G., and Tateyama, Y. (2019). Structures, Electronic States, and Reactions at Interfaces between LiNi$_{0.5}$Mn$_{1.5}$O$_4$ Cathode and Ethylene Carbonate Electrolyte: A First-Principles Study. **J. Phys. Chem. C**. 123: 2267.

Østergaard, T. M., Giordano, L., Castelli, I. E., Maglia, F., Antonopoulos, B. K., Shao-Horn, Y., and Rossmeisl, J. (2018). Oxidation of Ethylene Carbonate on Li Metal Oxide Surfaces. **J. Phys. Chem. C**. 122: 10442.

Pan, Y., Zhang, Y., Parimalam, B. S., Nguyen, C. C., Wang, G., and Lucht, B. L. (2017). Investigation of the solid electrolyte interphase on hard carbon electrode for sodium ion batteries. **J. Electroanal. Chem.** 799: 181.

Park, Y., Shin, D.-S., Woo, S. H., Choi, N. S., Shin, K. H., Oh, S. M., Lee, K. T., and Hong, S. Y. (2012). Sodium Terephthalate as an Organic Anode Material for Sodium Ion Batteries. **Adv. Mater.** 24: 3562.

Payne, R., and Theodorou, I. E. (1972). Dielectric properties and relaxation in ethylene carbonate and propylene carbonate. **J. Phys. Chem.** 76: 2892.

Peled, E. (1979a). The Electrochemical Behavior of Alkali and Alkaline Earth Metals in Nonaqueous Battery Systems—The Solid Electrolyte Interphase Model. **J. Electrochem. Soc.** 126: 2047.

Peled, E. (1979b). The Electrochemical Behavior of Alkali and Alkaline Earth Metals in Nonaqueous Battery Systems—The Solid Electrolyte Interphase Model. **J. Electrochem. Soc.** 126: 2047.

Peled, E., Golodnitsky, D., Ardel, G., and Eshkenazy, V. (1995a). The sei model—application to lithium-polymer electrolyte batteries. **Electrochim. Acta**. 40: 2197.

Peled, E., Golodnttsky, D., Ardel, G., Menachem, C., Bar Tow, D., and Eshkenazy, V. (1995b). The Role of SEI in Lithium and Lithium Ion Batteries. **Mater. Res. Soc. Symp. Proc.** 393: 209.

Peled, E., and Menkin, S. (2017). Review—SEI: Past, Present and Future. **J. Electrochem. Soc.** 164: A1703.

Ponrouch, A., Marchante, E., Courty, M., Tarascon, J.-M., and Palacín, M. R. (2012). In search of an optimized electrolyte for Na-ion batteries. **Energy Environ. Sci.** 5: 8572.

Purushotham, U., Takenaka, N., and Nagaoka, M. (2016). Additive effect of fluoroethylene and difluoroethylene carbonates for the solid electrolyte interphase film formation in sodium-ion batteries: a quantum chemical study. **RSC Adv.** 6: 65232.

Qin, X., Balbuena, P. B., and Shao, M. (2019). First-Principles Study on the Initial Oxidative Decompositions of Ethylene Carbonate on Layered Cathode Surfaces of Lithium-Ion Batteries. **J. Phys. Chem. C**. 123: 14449.

Que, L.-F., Yu, F.-D., Wang, Z.-B., and Gu, D.-M. (2018). Pseudocapacitance of TiO_{2-x}/CNT Anodes for High-Performance Quasi-Solid-State Li-Ion and Na-Ion Capacitors. **Small**. 14: 1704508.

Raccichini, R., Varzi, A., Passerini, S., and Scrosati, B. (2015). The role of graphene for electrochemical energy storage. **Nature Materials**. 14: 271.

Shakourian-Fard, M., Kamath, G., Smith, K., Xiong, H., and Sankaranarayanan, S. K. R. S. (2015). Trends in Na-Ion Solvation with Alkyl-Carbonate Electrolytes for Sodium-Ion Batteries: Insights from First-Principles Calculations. **J. Phys. Chem. C**. 119: 22747.

Shao, Y., Xiao, J., Wang, W., Engelhard, M., Chen, X., Nie, Z., Gu, M., Saraf, L. V., Exarhos, G., Zhang, J.-G., and Liu, J. (2013). Surface-Driven Sodium Ion Energy Storage in Nanocellular Carbon Foams. **Nano Lett.** 13: 3909.

Song, J. Y., Wang, Y. Y., and Wan, C. C. (1999). Review of gel-type polymer electrolytes for lithium-ion batteries. **J. Power Sources**. 77: 183.

Song, K., Liu, C., Mi, L., Chou, S., Chen, W., and Shen, C. (2019). Recent Progress on the Alloy-Based Anode for Sodium-Ion Batteries and Potassium-Ion Batteries. **Small**. n/a: 1903194.

Soto, F. A., Yan, P., Engelhard, M. H., Marzouk, A., Wang, C., Xu, G., Chen, Z., Amine, K., Liu, J., Sprenkle, V. L., El-Mellouhi, F., Balbuena, P. B., and Li, X. (2017). Tuning the Solid Electrolyte Interphase for Selective Li- and Na-Ion Storage in Hard Carbon. **Adv. Mater.** 29: 1606860.

Stankovich, S., Piner, R. D., Chen, X., Wu, N., Nguyen, S. T., and Ruoff, R. S. (2006). Stable aqueous dispersions of graphitic nanoplatelets via the reduction of exfoliated graphite oxide in the presence of poly(sodium 4-styrenesulfonate). **J. Mater. Chem.** 16: 155.

Stankovich, S., Dikin, D. A., Piner, R. D., Kohlhaas, K. A., Kleinhammes, A., Jia, Y., Wu, Y., Nguyen, S. T., and Ruoff, R. S. (2007). Synthesis of graphene-based nanosheets via chemical reduction of exfoliated graphite oxide. **Carbon**. 45: 1558.

Takenaka, N., Suzuki, Y., Sakai, H., and Nagaoka, M. (2014). On Electrolyte-Dependent Formation of Solid Electrolyte Interphase Film in Lithium-Ion Batteries: Strong Sensitivity to Small Structural Difference of Electrolyte Molecules. **J. Phys. Chem. C**. 118: 10874.

Takenaka, N., Sakai, H., Suzuki, Y., Uppula, P., and Nagaoka, M. (2015). A Computational Chemical Insight into Microscopic Additive Effect on Solid Electrolyte Interphase Film Formation in Sodium-Ion Batteries: Suppression of Unstable Film Growth by Intact Fluoroethylene Carbonate. **J. Phys. Chem. C**. 119: 18046.

Takenaka, N., and Nagaoka, M. (2019). Microscopic Elucidation of Solid-Electrolyte Interphase (SEI) Film Formation via Atomistic Reaction Simulations: Importance of Functional Groups of Electrolyte and Intact Additive Molecules. **Chem. Rec.** 19: 799.

Tarascon, J. M., and Armand, M. (2001). Issues and challenges facing rechargeable lithium batteries. **Nature**. 414: 359.

Vaalma, C., Buchholz, D., Weil, M., and Passerini, S. (2018). A cost and resource analysis of sodium-ion batteries. **Nat. Rev. Mater.** 3: 18013.

Verma, P., Maire, P., and Novák, P. (2010). A review of the features and analyses of the solid electrolyte interphase in Li-ion batteries. **Electrochim. Acta**. 55: 6332.

Vollmer, J. M., Curtiss, L. A., Vissers, D. R., and Amine, K. (2004). Reduction Mechanisms of Ethylene, Propylene, and Vinylethylene Carbonates: A Quantum Chemical Study. **J. Electrochem. Soc.** 151: A178.

Wang, A., Kadam, S., Li, H., Shi, S., and Qi, Y. (2018). Review on modeling of the anode solid electrolyte interphase (SEI) for lithium-ion batteries. **Npj Comput. Mater.** 4: 15.

Wang, Y., Nakamura, S., Ue, M., and Balbuena, P. B. (2001). Theoretical Studies To Understand Surface Chemistry on Carbon Anodes for Lithium-Ion Batteries: Reduction Mechanisms of Ethylene Carbonate. **J. Am. Chem. Soc.** 123: 11708.

Wang, Y., Nakamura, S., Tasaki, K., and Balbuena, P. B. (2002). Theoretical Studies To Understand Surface Chemistry on Carbon Anodes for Lithium-Ion Batteries: How Does Vinylene Carbonate Play Its Role as an Electrolyte Additive? **J. Am. Chem. Soc.** 124: 4408.

Wang, Y., Liu, Y., Tu, Y., and Wang, Q. (2020). Reductive Decomposition of Solvents and Additives toward Solid-Electrolyte Interphase Formation in Lithium-Ion Battery. **J. Phys. Chem. C**. 124: 9099.

Xia, Q., Li, W., Miao, Z., Chou, S., and Liu, H. (2017). Phosphorus and phosphide nanomaterials for sodium-ion batteries. **Nano Res.** 10: 4055.

Xu, J., Wang, M., Wickramaratne, N. P., Jaroniec, M., Dou, S., and Dai, L. (2015). High-Performance Sodium Ion Batteries Based on a 3D Anode from Nitrogen-Doped Graphene Foams. **Adv. Mater.** 27: 2042.

Xu, K. (2004). Nonaqueous Liquid Electrolytes for Lithium-Based Rechargeable Batteries. **Chem. Rev.** 104: 4303.

Xu, K. (2014). Electrolytes and Interphases in Li-Ion Batteries and Beyond. **Chem. Rev.** 114: 11503.

Yabuuchi, N., Kubota, K., Dahbi, M., and Komaba, S. (2014). Research Development on Sodium-Ion Batteries. **Chem. Rev.** 114: 11636.

Yoo, H. D., Shterenberg, I., Gofer, Y., Gershinsky, G., Pour, N., and Aurbach, D. (2013). Mg rechargeable batteries: an on-going challenge. **Energy Environ. Sci.** 6: 2265.

Young, J., and Smeu, M. (2018a). Ethylene Carbonate-Based Electrolyte Decomposition and Solid-Electrolyte Interphase Formation on Ca Metal Anodes. **J. Phys. Chem. Lett.** 9: 3295.

Young, J., and Smeu, M. (2018b). Ethylene Carbonate-Based Electrolyte Decomposition and Solid–Electrolyte Interphase Formation on Ca Metal Anodes. **J. Phys. Chem. Lett.** 9: 3295.

Yu, L., Wang, L. P., Liao, H., Wang, J., Feng, Z., Lev, O., Loo, J. S. C., Sougrati, M. T., and Xu, Z. J. (2018). Understanding Fundamentals and Reaction Mechanisms of Electrode Materials for Na-Ion Batteries. **Small**. 14: e1703338.

Zhang, Y., Chen, L., Meng, Y., Xie, J., Guo, Y., and Xiao, D. (2016). Lithium and sodium storage in highly ordered mesoporous nitrogen-doped carbons derived from honey. **J. Power Sources**. 335: 20.

Zhao, J., Zhang, Y.-Z., Zhang, F., Liang, H., Ming, F., Alshareef, H. N., and Gao, Z. (2019). Partially Reduced Holey Graphene Oxide as High Performance Anode for Sodium-Ion Batteries. **Adv. Energy Mater.** 9: 1803215.

Zhong, X., Wu, Y., Zeng, S., and Yu, Y. (2018). Carbon and Carbon Hybrid Materials as Anodes for Sodium-Ion Batteries. **Chem.: Asian J.** 13: 1248.

CHAPTER II

THEORETICAL AND COMPUTATIONAL

APPROACHES

2.1   Density functional theory

First principles computations based on density functional theory (DFT) have been used for investigating a wide range of essential properties of batteries. DFT recast the intractable complexity of many body wave functions by assumes electron density is a fundamental property which corresponds to the normalized N-electron wave function. This accelerates the speed of the calculation as electron density is a function of only three (x, y, z) variables instead of a function of 3N variables for many body electron wave functions (with N number of atoms). DFT calculations solve the problem Schrodinger equation (Schrödinger, 1926) with some approximations. The Schrodinger equation that describes the quantum nature of matter is:

$$\hat{H}\Psi = E\Psi \tag{2.1}$$

where, $\hat{H}$ represents the Hamiltonian operator, which provides total energy of the system, Ψ is the wave function, and E is the eigenvalue obtained after applying Hamiltonian to the wave function. This Hamiltonian includes the energy related to electron and nucleus in an atom i.e.

$$\hat{H} = \hat{H}_e + \hat{H}_n \tag{2.2}$$

By taking Born-Oppenheimer approximation (Born and Oppenheimer, 1927), nucleus moves slowly than electron because of higher mass result in totally separated degree of freedom between them. Therefore, dynamics of atomic nuclei can be described by the following equation:

$$(\hat{H}_e + \hat{H}_n) \, \Psi_n\Psi_e = E\Psi_n\Psi_e \qquad (2.3)$$

The energy operator of the electronic part $\hat{H}_e$ is split into a sum of three contributions: the kinetic energy of the electrons, T; potential energy of all the nuclei, V_{NN}; the internal potential energy obtained because of the repulsion between individual electrons, U_{ee}; external potential energy due to the attraction between the electrons and nuclei, V_{Ne}; and the exchange and correlation potential energy, V_{xc}, due to Pauli exclusion principle and spin effects.

$$\hat{H} = -\nabla^2 + V_{NN} + U_{ee} + V_{Ne} + V_{xc} \qquad (2.4)$$

For many electron problem, Schrodinger equation is:

$$\hat{H}\Psi_e \, (r_1, r_2, r_3, r_4 \ldots r_N) = E\Psi_e \, (r_1, r_2, r_3, r_4 \ldots r_N) \qquad (2.5)$$

where, r_1, r_2, r_3, $r_4 \ldots r_N$ are the position of electrons with number 1, 2, 3, 4…N, respectively. For each electron, the total electronic energy with 3N variables (x, y, z) is calculated while solving Schrodinger equation. While performing the calculation for a molecule, the goal is to find a wave function which give minimum energy of the system. It can be obtained by minimizing the expectation or average value of the Hamiltonian. Therefore, wave functions are picked randomly on trial basis for calculations until the energy is minimized.

$$E = \min_{\psi} <\psi/\hat{H}|\psi> \qquad (2.6)$$

Because it is very complex and tedious task to solve the above equation with many body wave function, DFT approach was introduced by Hohenberg and Kohn in 1964 (Hohenberg and Kohn, 1964) and later modified by Kohn and Sham (Kohn and Sham, 1965). DFT applied to a system makes its solution more realistic and simple. According to them, the electron density contains all the information, which is a function of only three coordinates (x, y, and z). Therefore, instead of using trial wave function for energy minimization, they minimize the potential energy of interaction between nuclei and electron by considering electron density.

$$E = min_n \int V_n(\vec{r}) n(\vec{r}) d^3\vec{r} + (-\nabla^2 + V_{NN} + U_{ee} + V_{xc}) \qquad (2.7)$$

2.2 Exchange correlation energy functional

In Kohn-Sham equation, it is difficult to obtain the exact exchange correlation potential energy functional (V_{xc}) as it depends on the electron density at each point in space while other potential energies are the columbic interaction between electrons and nuclei. The exchange interaction arises because of the repulsion between electrons having parallel spins while correlation arises because of the mutual coulombic repulsion between electrons with antiparallel spin. The V_{xc} is very complex functional, and therefore some approximations are required for its calculation. Local density approximation (LDA) (Perdew and Zunger, 1981) local spin density approximation (LSDA) (Wang and Perdew, 1991), generalized gradient approximation (GGA) (Perdew *et al.*, 1996c) and PerdewBurke-Ernzerhof exchange correlation (PBE) (Perdew *et al.*, 1996a) are some of the commonly used approximations for exchange correlation energy functional. LDA applies in DFT where V_{xc} at some position r is

computed exclusively from the electron density at that position. It calculates V_{xc} for the system by assuming uniform electron density everywhere in space. LDA is the simplest approximation to V_{xc}, where the exchange-correlation energy per particle is taken to be equal to that of a uniform electron gas of the same electron density, at each point in space. However, there can be an associated variation in energy with different in electrons spin; therefore, it becomes important to consider non-degeneracy in spin using LSDA. In this method, the XC functional depends on the spin densities, $\rho_\alpha(r)$ and $\rho_\beta(r)$, which are allowed to be different. However, it is unreasonable to assume that the molecules will always possess uniform distribution of electron density. Therefore, GGA considered that the functional are dependent on electron density and its first spatial gradient, resulting in a more accurate description of exchange and correlation.

GGA is a successful exchange correlation functional for small molecules. However, the approximation proved to be a failure for long-range interactions, as in the case of metals. Therefore, PBE uses gradient correction in LSDA approximation which can be used in case of delocalized electrons in uniform gas distribution (metals). PBE correlation considers short- and long-range interactions between the electrons in a system. The long-range interactions are important when dealing with lattice structure in battery materials. The physical and chemical properties of a material depend on its structure; therefore, evaluation of the long-range interactions between the electrons should be included during first-principles study.

2.3   Dispersion factors

In batteries, the anode material generally consists of graphite, graphene, and its analogs. The structure is layered and sparsely packed (Cooper *et al.*, 2010). Therefore, electron dispersion forces such as van der Waals interaction and London dispersion forces becomes prominent for determining the structures and properties of the electrode materials (Klimeš and Michaelides, 2012). Van der Waals interaction is distance-dependent attractive force between atoms, molecules, and electrons. It is a long-range force and is present in almost all the electronic systems (Kannemann and Becke, 2010). London dispersion forces is a type of van der Waals interaction which occurs when the electronic charge density is present at a particular location creating a negatively charge center in the molecule. This negative end generates the instantaneous dipole in the surrounding molecules by attracting their positive ends. Although van der Waals interaction originates from the electron correlation factor, however, DFT often fail to describe the dispersion component of the van der Waals energies, which arise from the response of electrons to instantaneous charge density fluctuations and it does not consider any long-range van der Waals interactions. Therefore, it becomes important to add some empirical corrections in DFT equation in order to improve its overall chemical accuracy (Davis *et al.*, 2015). The basic requirement for any DFT dispersion is that it should give a reasonable $-1/r^6$ asymptotic behavior of interaction between particles in gas phase, where r is the distance between the particles (Yang *et al.*, 2014). A simple approach is to add the additional dispersion energy term which accounts for the missing long-range attraction, into the computed DFT energies.

$$E_{tot} = E_{DFT} + E_{Dis} \qquad (2.8)$$

where, E_{tot}, E_{DFT}, and E_{Dis} are the total energy, energy calculated from Kohn-Sham equation with a given exchange correlation parameter, and dispersion energy, respectively. The dispersion interaction term is generalized as:

$$E_{Dis} = -\sum_{j=i+1}^{N} \frac{C_6^{ij}}{R_{ij}^6} \tag{2.9}$$

where, C_6 is the pairwise dispersion coefficients and R is the interatomic distance for each atom pair contributing to E_{dis}. The most popular dispersion variant is DFT-D because of its low cost and easy computation. However, DFT-D does not take into account for many body dispersion effect, faster decaying terms such as the C_8/r^8 or C_{10}/r^{10} interactions., and environmental effects (Dobson *et al.*, 2006). It does not tell us from where to obtain dispersion coefficient terms, and $\frac{C_6^{ij}}{R_{ij}^6}$ diverges for small separations (small value of R_{ij}), and this divergence must be removed. Further improvements in the dispersion corrected terms were made in 2006 by Grimme referred to as DFT-D2 (Grimme, 2006). In this approach, the dispersion coefficient term is calculated from ionization potentials and static polarizabilities of isolated atoms. However, there are some problems in DFT-D2 such as the dispersion coefficient for some elements still needs to be calculated, and the interaction energy/dispersion energy depends on exchange correlation functional used leading to the sensitive of the constant to the choice of exchange correlation functional. Therefore, dispersion energy is further improvised using the general formula:

$$E_{Dis} = -S6 \sum_{\substack{i=N-1 \\ j=i+1 \\ i=1}}^{j=N} \frac{C_6^{ij}}{R_{ij}^6} f_d(R_{ij}) \tag{2.10}$$

where, N is the total number of atoms, C_6^{ij} is the dispersion coefficient, R_{ij} is the bond distance for atom pair ij, and S_6 is a scaling factor, dependent on the exchange

functional. A damping factor, f_d, is used to prevent singularities at small distances. However, still there is no consideration of environmental effects such as the number of neighbors possesses by each particle. The number of neighbors has a direct effect on the dispersion coefficient because with increase in number of neighbor, the particle will be squeezed, and therefore the coefficient will also decrease. Therefore, DFT-D3 variant which is characterized by higher accuracy, a broader range of applicability, and less empiricism compared to the DFT-D2 was introduced by Grimme (Grimme *et al.*, 2010) to overcome these issues. Further improvisation was done by developing methods such as BJ model (Becke and Johnson, 2005), vdw-DF and vdw-DF2 (Lee *et al.*, 2010; Murray *et al.*, 2009) and random phase approximations (Furche, 2001) for the dispersion correction terms.

2.4   Plane wave basis sets and integration methods

A plane wave is a constant-frequency wave whose wave fronts are parallel infinite, generally used for periodic functions whereas a basis set is the representation of electronic wave function in DFT. A basis set can be composed of atomic orbitals or plane wave. The material used in batteries consists of lattices, unit cells indicating existence of periodic properties. Therefore, it is the plane wave basis set which is used for the study of these materials. There are certain tools packages such as Quantum expresso (Giannozzi *et al.*, 2009), SEISTA code (Soler *et al.*, 2002), Cambridge Serial Total Energy Package (Clark *et al.*, 2005) and Vienna Ab initio Simulation (Kresse and Furthmüller, 1996b) which uses plane wave as a basis set. Now, the plane wave consists of infinite number of wave front; therefore, to reduce the plane wave basis set to a finite

size, only those plane waves are included whose kinetic energy is less than the specified

cut-off energy. The specified cut-off energy is calculated using (Alloul, 2011):

$$E_{cutoff} = \frac{\hbar^2}{2m}|k|^2 \qquad (2.11)$$

where, k is a wave vector while m is an integer. Since, E_{cutoff} affects the accuracy of the

calculations; therefore, it should be high enough until the respective properties are

converged. In a periodic system, Bloch theorem (Bloch, 1929; Kronig *et al.*, 1931) is

used to express a wave function as a product of plane wave and a function of periodicity

of lattice.

$$\psi(r) = u(r)e^{ikr} \qquad (2.12)$$

where, ψ(r) is a wave function, u(r) is the periodic function, and e^{ikr} is the expression

for plane wave, k is the wave vector. Because wavevectors are measured in units of

1/length, they describe points in reciprocal space. The periodic function for all the

combination of wave vector lies in Brillouin zone (Bouckaert *et al.*, 1936) which itself

is a Wigner-Seitz cell in a reciprocal lattice. The sum over wave functions can be

expressed as integrals over the Brillouin zone. Such integrals are numerically estimated

by sampling the Brillouin zone at a finite number of k-points. Therefore, Monkhorst-

Pack grid (Monkhorst and Pack, 1976) method is used to perform such calculations.

Monkhorst-Pack grid method assumes that the k-points forming rectangular grid of a

definite and finite dimension are evenly placed in Brillouin zone. The size of the grid

is approximated according to the system under study and the best obtained convergence.

Bloch tetrahedron method (Blöchl *et al.*, 1994) is another way of integrating Brillouin

zone. In this method, the irreducible part of the reciprocal space in Brillouin zone is

divided into non-overlapping and same volume tetrahedra. The energy quantity is

integrated within the cells present in the tetrahedron. However, this method does not show variation in energy with the difference in the occupancy of valence and conduction bands in metals. Therefore, smearing methods such as Gaussian (Björkman and Grånäs, 2011) is explored which shows variation with respect to the occupancies. In Gaussian broadening smearing integration, the energy associated with the particles having weak interaction, which are present in the material/metal, is smeared out to a Gaussian function, which itself represent the probability density functions of a normal distributed random variable.

In metals, all the electrons reside in the valence band within the Fermi energy level at absolute zero temperature. On increasing the temperature, some of the electrons can occur above the Fermi level, and at high temperature, electrons reach the conduction band leading to flow of electric current. Therefore, there is discontinuity in the filling of energy bands with electrons and hence in k-space with filled and unfilled states at absolute zero temperature. This requires large number of k-points for the study because of which the convergence of the system becomes very slow. To solve the problem, Fermi-Dirac (Aarons *et al.*, 2016) broadening sampling integration method is used. Fermi-Dirac smearing involves the temperature of interest in the system and approximates the step function by Fermi-Dirac distribution:

$$f(E) = \frac{1}{e^{(E-E_F)/kT}+1} \tag{2.13}$$

When T approaches absolute zero temperature, the function approaches step function. However, this approach has a drawback of the presence of reduced occupation probability in the states with energies smaller than the Fermi energy. This smaller energy than that of Fermi energy is not compensated by the occupation probability of

the newly introduced states with energies higher than the Fermi energy. To overcome this problem, MethfesselPaxton smearing (Methfessel and Paxton, 1989) gave new approximation of the delta function which on integration approximates the step function. The delta function is approximated by multiplying the Hermite polynomials with the Gaussian.

$$\delta(x) = \sum_n^N A_n H_{2n} e^{-x^2} \tag{2.14}$$

where, A_n is some coefficient, H_{2n} is Hermite polynomials, and e^{-x^2} is the Gaussian function. The delta function is associated with the potential which is zero everywhere in space except at a single point where it is infinity. It is generally used when the two conducting surfaces are place close together and the interface between them acts as a barrier for the electron, which is approximated by delta function indicating its importance in metal-ion battery investigation.

The relaxation of the atomic position in the lattice and obtaining structure with minimum energy for geometry optimization is a very important task for the study of materials. To obtain the atomic structures with minimum potential energy, various optimization methods such as steepest descent, conjugated gradient, Newton-Raphson and quasi-Newton are used (Nocedal and Wright, 2006). Broyden-Fletcher-Goldfarb-Shanno algorithm is one of the quasi-Newton methods generally used for atomic optimization of lattices while designing material for metal-ion battery (Banerjee *et al.*, 2016; Li *et al.*, 2014; Shu *et al.*, 2010; Wang *et al.*, 2013). The basic idea behind these methods is that the function or their first- and second-order derivatives associated with the atoms should be zero. Initially a geometry or structure of a molecule is selected which contains some atomic positions having 3N coordinates. With each position, there

is an associated function for which a gradient can be obtained by drawing a tangent at that point. The displacement in the position is made until the gradient associated with the function becomes zero. Newton method approximates second-order function by considering the gradient factor and the second-order derivative. The second-order derivative function is approximated by using a quadratic. The second-order derivative approximations are faster than the first-order; therefore, Newton method gives faster geometric optimization without compromising to the results. Newton's method uses the gradient and the Hessian matrix of second derivatives for the function to be minimized. However, these methods are expensive; therefore, quasi-Newton method was developed in which the Hessian matrix is not computed. The Hessian is updated by analyzing successive gradient vectors, and these methods are a generalization of the secant method to find the root of the first derivative for multidimensional problems.

2.5   Pseudo-potential and projector augmented wave method

A molecule consists of core and valence electrons which affect the properties of the respective molecule. Core electrons are closer to the nucleus and tightly bound to it while valence electrons are loosely bound. Therefore, it is the valence electrons which are majorly responsible and involved in the chemical and physical properties of the molecule (Li *et al.*, 2014). There is a reduction in the nodes in case of valence electron wave function (Ψ_{ps}) as compared with the all electron wave function (Ψ) (Troullier and Martins, 1991). Therefore, wave function for all electron will involve large number of basis set. Because all the physical and chemical properties of a system depend on the valence electron, therefore, it becomes important to reduce the atomic potential to only

valence electron while the core electrons are frozen. This is the idea behind pseudopotential which reduces the size of the plane wave basis set but reproduces the similar wave function outside the core region corresponding to the lower cut-off energy. The wave functions associated with the valence electron have rapid oscillation near the core leading to large number of Fourier components involvement in the wave function. Therefore, projected augmented wave (PAW) method was developed by Bloch to accurately calculate the electronic structures of a material (Blöchl, 1994) and reduce the number of Fourier components. It not only retains the original nodal behavior of the wave function for valence electrons but also includes the upper core electrons in the self-consistent iterations (Holzwarth *et al.*, 1997). PAW smoothens the rapid oscillating wave function to calculate the respective properties of the system which is computationally an efficient approach. PAW assumes that the potential is spherically symmetric near nuclei or core region and constant in the interstitial region which smoothens the wave function. In the core region, the solution for the spherically symmetric wave function will match the Schrodinger solution, whereas at the interstitial site, it will be a plane wave function. The smooth wave functions are obtained from the original wave function with similar nodal behavior by assuming three set of function for each atom; an all electron basis function , $\varphi_i^a(r)$, pseudo basis function, $\tilde{\varphi}_i^a(r)$, and projector function, $\tilde{p}_i^a(r)$. Bloch said that all electron and pseudo basis functions are chosen such that:

$$\varphi_i^a(r) = \tilde{\varphi}_i^a(r) \; for \; r \geq r_c^a \tag{2.15}$$

where; r_c^a is the core electron radius for an atom a. Therefore, the above equation depicts that the all electron basis is equal to pseudo function only when the radius is taken above the core radius. $\varphi_i^a(r)$, $\tilde{\varphi}_i^a(r)$ are never evaluated above r_c^a, and $\tilde{p}_i^a(r)$

vanishes for radius greater than r_c^a. The Bloch wave function can be obtained from the smooth wave function, $\tilde{\psi}_{nk}(r)$ using below equation:

$$\psi_{nk}(r) = \tilde{\psi}_{nk}(r) + \sum_{ai}[\varphi_i^a(r - R^a) - \tilde{\varphi}_i^a(r - R^a)]\tilde{p}_i^a|\tilde{\psi}_{nk} \qquad (2.16)$$

Where, R^a is the atomic position within the unit cell. In PAW formalism, valence electron density is calculated using below equation:

$$n(r) = \tilde{n}(r) + n^1(r) - \tilde{n}^1(r) \qquad (2.17)$$

where, $n(r)$ is the valence electron density, $\tilde{n}(r)$ is the pseudo density, and the last two terms are the correction term to obtain the nodal behavior similar to that of oscillating wave function. Similarly, energy of valence electrons is calculated using:

$$E(r) = \tilde{E}(r) + E^1(r) - \tilde{E}^1(r) \qquad (2.18)$$

where, $E(r)$ is the energy of valence electrons interacting with themselves assuming core electrons are frozen, $\tilde{E}(r)$ is the smooth density function thought the unit cell, and $E^1(r)$ and $\tilde{E}^1(r)$ are evaluated over all integrals involving valence density contributions confined for sphere radius with r_c^a. It can be observed from the literature that the PAW has wide application for understanding the properties of electrode materials used in batteries.

2.6 Minimum energy path

Minimum energy path (MEP) is a path that connects the initial and final state of the process, and it is assumed that the forces acting on the atoms present in the path will always be pointing along the path. The maxima on this MEP is the saddle point on the potential energy surface. MEP consists of more than one maxima and minima;

therefore, nudge elastic band (NEB) approximation is applied to obtain the accurate saddle point. NEB is used to find the saddle points and MEP between the reactants and products. In this method, a set of "images" of the system that lie approximately along the minimal energy path is constructed between the initial state to the finial state. NEB optimizes the intermediate images along the diffusion path. Each image finds the lowest energy possible in that path (MEP) without interfering with other replicated images. This constrained optimization is done by adding spring forces along the band between the images and by projecting out the component of the force due to the potential perpendicular to the band. The saddle point is determined as the maximum energy configuration along the minimal energy path, but still there is some inaccuracy in finding the maxima in MEP as depicted in Figure 2.1. Therefore, a small modification in NEB is made by CI-NEB. In CI-NEB, the true force at the image along the tangent is inverted rather than feeling the spring forces along the band. In this way, the image tries to maximize its energy along the band and minimize in all other directions. This image converges at the exact saddle point.
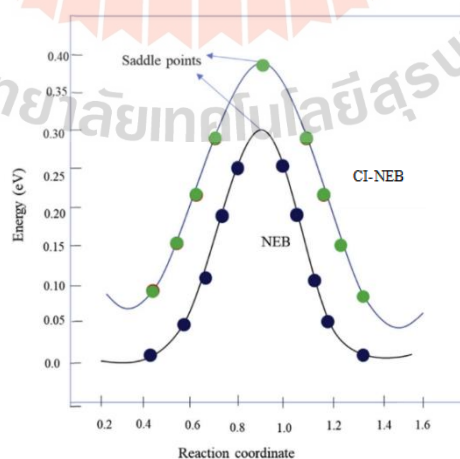
Figure 2.1 Saddle points obtained from NEB and CI-NEB modifications. NEB, nudge elastic band; CI-NEB, climbing image nudged elastic band (Ladha, 2019).

2.7 A Summary of computational details

All computations carried out in this work are based on fully periodic planewave DFT calculations as implemented in the Vienna Ab Initio Simulation Package (VASP 5.4) (Kresse and Furthmüller, 1996a). The exchange-correlation functional is approximated using the generalized gradient approximation with the Purdue-Burke-Ernzerhof (PBE) functional (Perdew *et al.*, 1996b) with the correction method of Grimme *et al.* (DFT-D3) (Grimme *et al.*, 2010). The projector augmented wave method (PAW) (Blöchl, 1994) was used to describe interactions between core electron potentials and valence electron wavefunction which were expanded at the cutoff of 500 eV. The treated valence electrons are O $2s^22p^4$, C $2s^22p^2$, H $1s^1$, and Na $2p^63s^1$. We used the k-point sampling in the Brillouin zone as Γ-centered k-point grids of $5 \times 5 \times 1$ and all atoms were allowed to relax. Gaussian smearing with a width of 0.1 eV was used. Spin polarization was considered in all calculations. Structural relaxation is carried out until residual forces were less than 0.02 eV/Å and energies are converged to within 1×10^{-6} eV per atom. Transition-state structures and minimum-energy pathways for EC decomposition reactions are determined using the climbing image nudged elastic band (CI-NEB) (Henkelman *et al.*, 2000) and dimer methods (Henkelman and Jónsson, 1999). The transition-state structures were confirmed by vibrational analysis where they should exhibit single strong imaginary frequency. The electronic charges is performed using Bader charge analysis (Henkelman *et al.*, 2006; Sanville *et al.*, 2007; Tang *et al.*, 2009). To study EC decomposition reactions on graphene surface, pristine graphene (*p*-graphene) was modelled as a single-layer graphene consisting of 5×5 supercell with a vacuum gap of 16 Å applied in a vertical z-direction to avoid spurious periodic images interactions and, as shown in Figure 2.2(a).

The effect of epoxy on the surface reactions is evaluated by adding an epoxy group on graphene resulting in a coverage of 0.02 monolayer (Figure 2.2(b)). The introduction of epoxy group causes significant disruption of graphene sheet and Bader charge analysis shown that the epoxy group withdraw 0.81 e$^-$ from graphene sheet. Although the single layer graphene does not represent actual structure of carbon anodes of SIBs, it can avoid the effect of the graphitic interlayer distance and morphology, and take into account only the effect of epoxy group on the decomposition mechanisms (Bommier *et al.*, 2019; Jensen *et al.*, 2020; Li *et al.*, 2017).
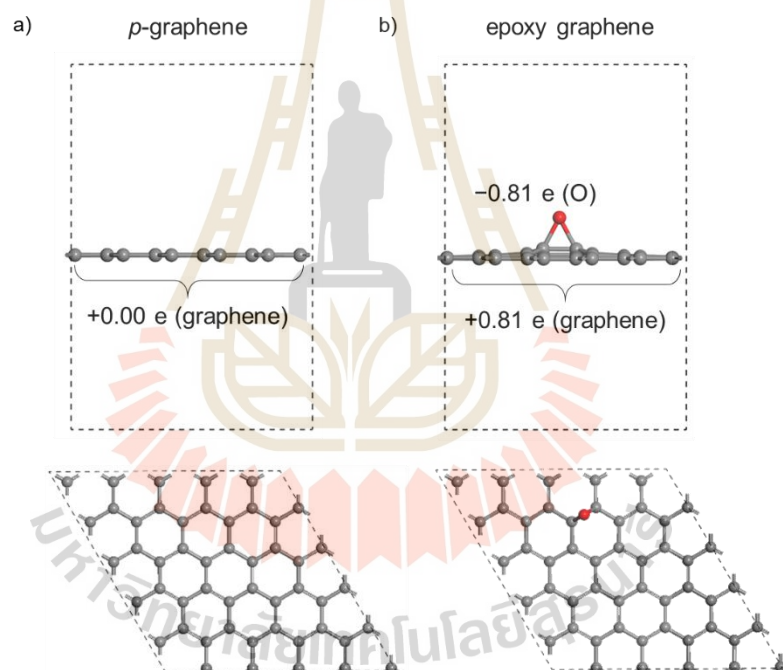
Figure 2.2 Top view (top panel) and side view (bottom panel) of a) 5 × 5 pristine graphene supercell structure and b) 5 × 5 graphene supercell structure decorated with a single epoxy group and corresponding Bader charge of graphene sheet and epoxy group. Grey and red sphere represent C and O species, respectively.

2.8 References

Aarons, J., Sarwar, M., Thompsett, D., and Skylaris, C.-K. (2016). Perspective: Methods for large-scale density functional calculations on metallic systems. **J. Chem. Phys.** 145: 220901.

Alloul, H. (2011). **Introduction to the Physics of Electrons in Solids**. 1 ed: Springer-Verlag Berlin Heidelberg.

Banerjee, S., Neihsial, S., and Pati, S. K. (2016). First-principles design of a borocarbonitride-based anode for superior performance in sodium-ion batteries and capacitors. **J. Mater. Chem. A**. 4: 5517.

Becke, A. D., and Johnson, E. R. (2005). Exchange-hole dipole moment and the dispersion interaction. **J. Chem. Phys.** 122: 154104.

Björkman, T., and Grånäs, O. (2011). Adaptive smearing for Brillouin zone integration. **Int. J. Quantum Chem.** 111: 1025.

Bloch, F. (1929). Über die Quantenmechanik der Elektronen in Kristallgittern. **Z. Phys.** 52: 555.

Blöchl, P. E. (1994). Projector augmented-wave method. **Phys. Rev. B**. 50: 17953.

Blöchl, P. E., Jepsen, O., and Andersen, O. K. (1994). Improved tetrahedron method for Brillouin-zone integrations. **Phys. Rev. B**. 49: 16223.

Bommier, C., Ji, X., and Greaney, P. A. (2019). Electrochemical Properties and Theoretical Capacity for Sodium Storage in Hard Carbon: Insights from First Principles Calculations. **Chem. Mater.** 31: 658.

Born, M., and Oppenheimer, R. (1927). Zur Quantentheorie der Molekeln. **Ann. Phys. (Berl.)**. 389: 457.

Bouckaert, L. P., Smoluchowski, R., and Wigner, E. (1936). Theory of Brillouin Zones and Symmetry Properties of Wave Functions in Crystals. **Phys. Rev.** 50: 58.

Clark, S., Segall, M., Pickard, C., Hasnip, P., Probert, M., Refson, K., and Payne, M. (2005). First principles methods using CASTEP. **Z. Kristallogr. Cryst. Mater.** 220:

Cooper, V. R., Kong, L., and Langreth, D. C. (2010). Computing dispersion interactions in density functional theory. **Phys. Procedia**. 3: 1417.

Davis, J. B. A., Baletto, F., and Johnston, R. L. (2015). The Effect of Dispersion Correction on the Adsorption of CO on Metallic Nanoparticles. **J. Phys. Chem. A**. 119: 9703.

Dobson, J. F., White, A., and Rubio, A. (2006). Asymptotics of the Dispersion Interaction: Analytic Benchmarks for van der Waals Energy Functionals. **Phys. Rev. Lett.** 96: 073201.

Furche, F. (2001). Molecular tests of the random phase approximation to the exchange-correlation energy functional. **Phys. Rev. B**. 64: 195120.

Giannozzi, P., Baroni, S., Bonini, N., Calandra, M., Car, R., Cavazzoni, C., Ceresoli, D., Chiarotti, G. L., Cococcioni, M., Dabo, I., Dal Corso, A., de Gironcoli, S., Fabris, S., Fratesi, G., Gebauer, R., Gerstmann, U., Gougoussis, C., Kokalj, A., Lazzeri, M., Martin-Samos, L., Marzari, N., Mauri, F., Mazzarello, R., Paolini, S., Pasquarello, A., Paulatto, L., Sbraccia, C., Scandolo, S., Sclauzero, G., Seitsonen, A. P., Smogunov, A., Umari, P., and Wentzcovitch, R. M. (2009). QUANTUM ESPRESSO: a modular and open-source software project for quantum simulations of materials. **J. Phys.: Condens. Matter**. 21: 395502.

Grimme, S. (2006). Semiempirical GGA-type density functional constructed with a long-range dispersion correction. **J. Comput. Chem.** 27: 1787.

Grimme, S., Antony, J., Ehrlich, S., and Krieg, H. (2010). A consistent and accurate ab initio parametrization of density functional dispersion correction (DFT-D) for the 94 elements H-Pu. **J. Chem. Phys.** 132: 154104.

Henkelman, G., and Jónsson, H. (1999). A dimer method for finding saddle points on high dimensional potential surfaces using only first derivatives. **J. Chem. Phys.** 111: 7010.

Henkelman, G., Uberuaga, B. P., and Jónsson, H. (2000). A climbing image nudged elastic band method for finding saddle points and minimum energy paths. **J. Chem. Phys.** 113: 9901.

Henkelman, G., Arnaldsson, A., and Jónsson, H. (2006). A fast and robust algorithm for Bader decomposition of charge density. **Comput. Mater. Sci.** 36: 354.

Hohenberg, P., and Kohn, W. (1964). Inhomogeneous Electron Gas. **Phys. Rev.** 136: B864.

Holzwarth, N. A. W., Matthews, G. E., Dunning, R. B., Tackett, A. R., and Zeng, Y. (1997). Comparison of the projector augmented-wave, pseudopotential, and linearized augmented-plane-wave formalisms for density-functional calculations of solids. **Phys. Rev. B**. 55: 2005.

Jensen, A. C. S., Olsson, E., Au, H., Alptekin, H., Yang, Z., Cottrell, S., Yokoyama, K., Cai, Q., Titirici, M.-M., and Drew, A. J. (2020). Local mobility in electrochemically inactive sodium in hard carbon anodes after the first cycle. **J. Mater. Chem. A**. 8: 743.

Kannemann, F. O., and Becke, A. D. (2010). van der Waals Interactions in Density-Functional Theory: Intermolecular Complexes. **J. Chem. Theory Comput.** 6: 1081.

Klimeš, J., and Michaelides, A. (2012). Perspective: Advances and challenges in treating van der Waals dispersion forces in density functional theory. **J. Chem. Phys.** 137: 120901.

Kohn, W., and Sham, L. J. (1965). Self-Consistent Equations Including Exchange and Correlation Effects. **Phys. Rev.** 140: A1133.

Kresse, G., and Furthmüller, J. (1996a). Efficiency of ab-initio total energy calculations for metals and semiconductors using a plane-wave basis set. **Comput. Mater. Sci.** 6: 15.

Kresse, G., and Furthmüller, J. (1996b). Efficient iterative schemes for ab initio total-energy calculations using a plane-wave basis set. **Phys. Rev. B**. 54: 11169.

Kronig, R. D. L., Penney, W. G., and Fowler, R. H. (1931). Quantum mechanics of electrons in crystal lattices. **Proc. R. Soc. A**. 130: 499.

Ladha, D. G. (2019). A review on density functional theory–based study on two-dimensional materials used in batteries. **Mater. Today Chem.** 11: 94.

Lee, K., Murray, É. D., Kong, L., Lundqvist, B. I., and Langreth, D. C. (2010). Higher-accuracy van der Waals density functional. **Phys. Rev. B**. 82: 081101.

Li, G., Jiang, D., Wang, H., Lan, X., Zhong, H., and Jiang, Y. (2014). Glucose-assisted synthesis of $Na_3V_2(PO_4)_3$/C composite as an electrode material for high-performance sodium-ion batteries. **J. Power Sources**. 265: 325.

Li, Z., Bommier, C., Chong, Z. S., Jian, Z., Surta, T. W., Wang, X., Xing, Z., Neuefeind, J. C., Stickle, W. F., Dolgos, M., Greaney, P. A., and Ji, X. (2017). Mechanism

of Na-Ion Storage in Hard Carbon Anodes Revealed by Heteroatom Doping. **Adv. Energy Mater.** 7:

Methfessel, M., and Paxton, A. T. (1989). High-precision sampling for Brillouin-zone integration in metals. **Phys. Rev. B**. 40: 3616.

Monkhorst, H. J., and Pack, J. D. (1976). Special points for Brillouin-zone integrations. **Phys. Rev. B**. 13: 5188.

Murray, É. D., Lee, K., and Langreth, D. C. (2009). Investigation of Exchange Energy Density Functional Accuracy for Interacting Molecules. **J. Chem. Theory Comput.** 5: 2754.

Nocedal, J., and Wright, S. J. (2006). **Springer Series in Operations Research and Financial Engineering**. 2nd ed. New York: Springer.

Perdew, J. P., and Zunger, A. (1981). Self-interaction correction to density-functional approximations for many-electron systems. **Phys. Rev. B**. 23: 5048.

Perdew, J. P., Burke, K., and Ernzerhof, M. (1996a). Generalized Gradient Approximation Made Simple. **Phys. Rev. Lett.** 77: 3865.

Perdew, J. P., Burke, K., and Ernzerhof, M. (1996b). Generalized Gradient Approximation Made Simple. **Phys. Rev. Lett.** 77: 3865.

Perdew, J. P., Burke, K., and Wang, Y. (1996c). Generalized gradient approximation for the exchange-correlation hole of a many-electron system. **Phys. Rev. B**. 54: 16533.

Sanville, E., Kenny, S. D., Smith, R., and Henkelman, G. (2007). Improved grid-based algorithm for Bader charge allocation. **J. Comput. Chem.** 28: 899.

Schrödinger, E. (1926). Quantisierung als Eigenwertproblem. **Ann. Phys. (Berl.)**. 384: 361.

Shu, J., Yi, T.-F., Shui, M., Wang, Y., Zhu, R.-S., Chu, X.-F., Huang, F., Xu, D., and Hou, L. (2010). Comparison of electronic property and structural stability of $LiMn_2O_4$ and $LiNi_{0.5}Mn_{1.5}O_4$ as cathode materials for lithium-ion batteries. **Comput. Mater. Sci.** 50: 776.

Soler, J. M., Artacho, E., Gale, J. D., García, A., Junquera, J., Ordejón, P., and Sánchez-Portal, D. (2002). The SIESTA method forab initioorder-Nmaterials simulation. **J. Phys.: Condens. Matter**. 14: 2745.

Tang, W., Sanville, E., and Henkelman, G. (2009). A grid-based Bader analysis algorithm without lattice bias. **J. Phys.: Condens. Matter**. 21: 084204.

Troullier, N., and Martins, J. L. (1991). Efficient pseudopotentials for plane-wave calculations. **Phys. Rev. B**. 43: 1993.

Wang, W., Yu, C., Lin, Z., Hou, J., Zhu, H., and Jiao, S. (2013). Microspheric $Na_2Ti_3O_7$ consisting of tiny nanotubes: an anode material for sodium-ion batteries with ultrafast charge-discharge rates. **Nanoscale**. 5: 594.

Wang, Y., and Perdew, J. P. (1991). Spin scaling of the electron-gas correlation energy in the high-density limit. **Phys. Rev. B**. 43: 8911.

Yang, F., Sun, W., Li, Y., Yuan, H., Dong, Z., Li, H., Tian, J., Zheng, Y., and Zhang, J. (2014). Li_2FePO_4F and its metal-doping for Li-ion batteries: an ab initio study. **RSC Adv.** 4: 50195.

CHAPTER III

ETHYLENE CARBONATE DECOMPOSITION WITH

ONE Na ATOM ON *P*-GRAPHENE AND EPOXY

GRAPHENE SURFACES

3.1 Adsorption of Na atom on *p*-graphene and epoxy graphene

We firstly examined a Na atom adsorption on the *p*-graphene and epoxy graphene. Various initial adsorption sites were investigated (Figure 3.1). The adsorption energies of Na atom on graphene and epoxy graphene, $E_{ads,Na}$, were defined by Eq. (1):

$$E_{ads,n(Na)} = E_{Epoxy(Graphene)+Na} - E_{Epoxy(Graphene)} - (n \times E_{Na}) \quad (1)$$

where $E_{Epoxy(Graphene)+Na}$ is the total energy of the Na-adsorbed *p*-graphene or epoxy graphene system; $E_{Epoxy(Graphene)}$ is the total energy of the *p*-graphene or epoxy graphene sheet, and E_{Na} is the total energy of an isolated Na atom. The lower $E_{ads,Na}$ (more negative) indicates the stronger and more stable adsorption. The optimized structures and adsorption energies are shown in Figure 3.1. Three possible adsorption sites on the *p*-graphene were considered including hollow (in the middle of a C_6-ring), top (top of carbon site), and bridge (between C–C bond) sites. In accordance with previous studies (Liang *et al.*, 2017; Olsson *et al.*, 2019; Pašti *et al.*, 2018), the most stable adsorption site for Na adsorption on *p*-graphene is the hollow site with the

$E_{ads,Na}$ of −0.84 eV and the distance between Na atom and graphene sheet of 2.21 Å (Figure 3.1(b) and 3.1(e)). In addition, the Bader charge analysis (Figure 3.1(b)) shows that the Na atom donates 0.92 e⁻ to graphene sheet without any configurational distortion of graphene sheet (Pašti *et al.*, 2018).

The adsorption configurations for Na atom adsorption on the epoxy graphene is different from that on the *p*-graphene. The interaction of Na with epoxy group result in a slight shift of the Na atom position from previous adsorption sites on *p*-graphene, as depicted in Figure 3.1(d), 3.1(e), and 3.1(f). Therefore, two possible adsorption configurations were obtained by varying the position of the Na atom around epoxy group including the Na atom located slightly above the bridge site (Figure 3.1(d)) and between hollow and top site (Figure 3.1(e)). However, both configurations exhibit the same $E_{ads,Na}$ of −2.21 eV, which indicate negligible effects caused by the variation of the position of Na atom related to graphene sheet due to longer distance between Na atom and graphene sheet (2.76 Å vs 2.21 Å on *p*-graphene). The adsorption energy of Na on epoxy graphene of −2.21 eV is significantly lower than that on *p*-graphene because the electrostatic interaction between epoxy group and Na atoms. The charge analysis reveals that the Na atom donates 0.59 e⁻ to graphene sheet (total charge of +0.22 e⁻ on graphene sheet) and 0.31 e⁻ to epoxy group (total charge of −1.12 e⁻ on epoxy group)(Figure 3.1 (e)). The increase of charge on epoxy group cause the epoxide oxygen shifts from graphene bridge site to top site (Figure 3.1(d) and 3.1(e)) which is more stable than that without shifting of oxygen atom (Figure 3.1(f)) (Diklić *et al.*, 2019).
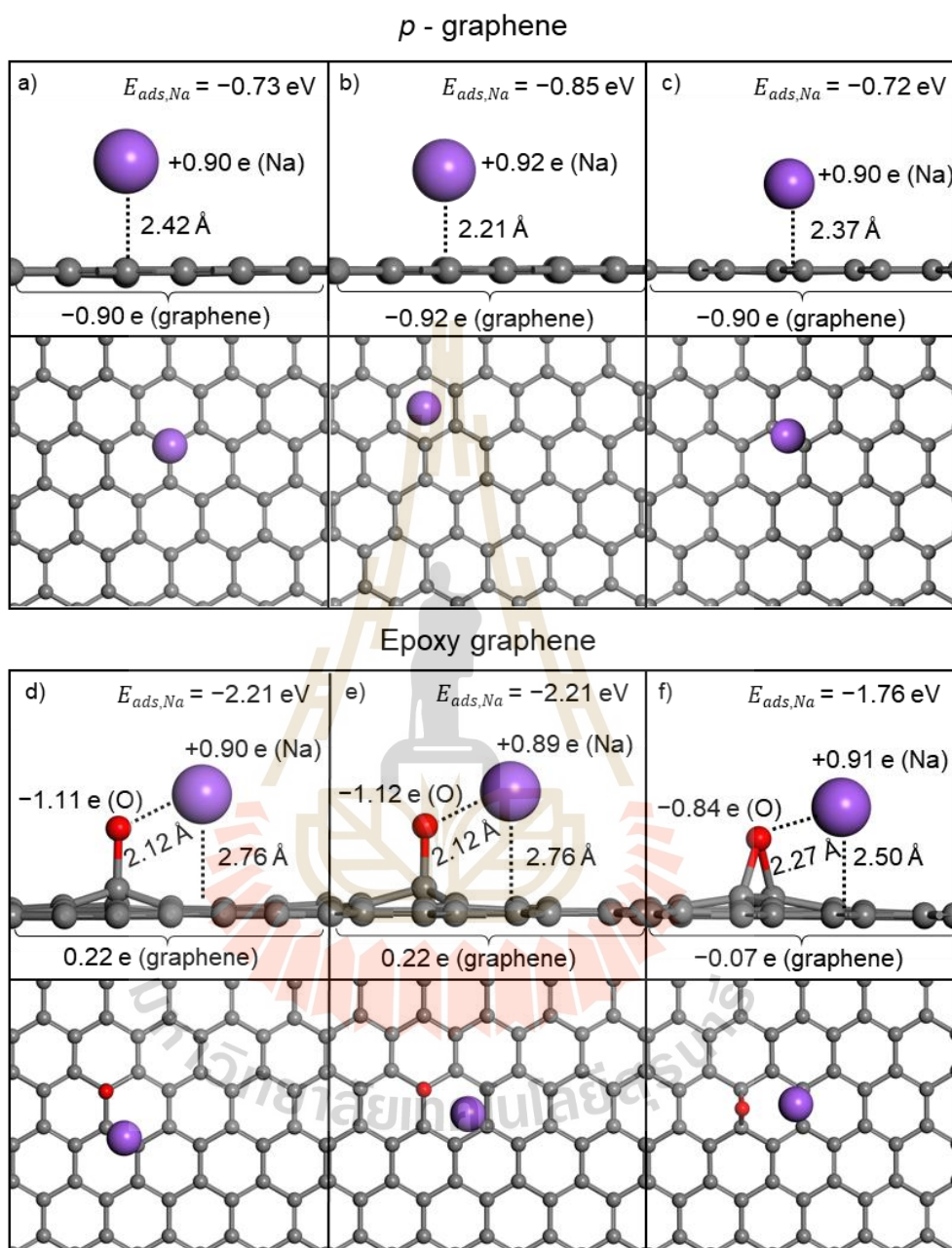
Figure 3.1 Optimized structures of different possible Na adsorption configurations on ((a), (b), and (c)) *p*-graphene and ((d), (e), and (f)) epoxy graphene.

3.2 Co-adsorption of Na atom and EC molecule on *p*-graphene and epoxy graphene

.   To investigate the EC decomposition mechanisms, one EC molecule was then placed onto the most stable adsorbed configurations of Na atom on graphene and epoxy graphene in perpendicular and parallel orientations to the surface (Figure 3.2). The co-adsorption energies, $E_{ads,Na+EC}$, of EC and Na adsorption on graphene and epoxy graphene were defined by Eq. (2):

$$E_{ads,Na+EC} = E_{Epoxy(Graphene)+Na+EC} - (E_{Epoxy(Graphene)} + E_{Na} + E_{EC}) \quad (2)$$

where $E_{Epoxy(Graphene)+Na+EC}$ is the total energy of EC and Na adsorption on graphene or epoxy graphene, $E_{Epoxy(Graphene)}$ is the total energy of the graphene or epoxy graphene sheet; E_{Na} is the total energy of an isolated Na atom, and E_{EC} is the total energy of an isolated EC molecule. On both surfaces, the structures of an EC ring being parallel to the surface give adsorption energies of −2.05 eV for *p*-graphene and −3.31 eV for epoxy graphene which are lower than these of vertical orientations of EC. The EC molecule binds to the Na ion through the O_C atoms with O_E atom slightly bend toward the Na as illustrated in Figure 3.2(a) and 3.2(b). As can be seen in Figure 3.2(e) and 3.2(f), the charge density distribution of EC molecule after adsorbed on both surfaces was investigated by the electron density difference, obtained by subtracting from the charge density of the total adsorbate system the sum of the charge densities of EC, Na atom and the clean surfaces, calculated using the same geometry as the adsorbate system. The charge density is depleted from C_C−O_C and C_E−O_E bonds and accumulate on O_C atom where it interacts with Na ion. Hence, the EC adsorption with planar

orientation on both surfaces were used as the starting point to investigate EC decomposition mechanism in the vicinity of 1 Na atom (1Na system).
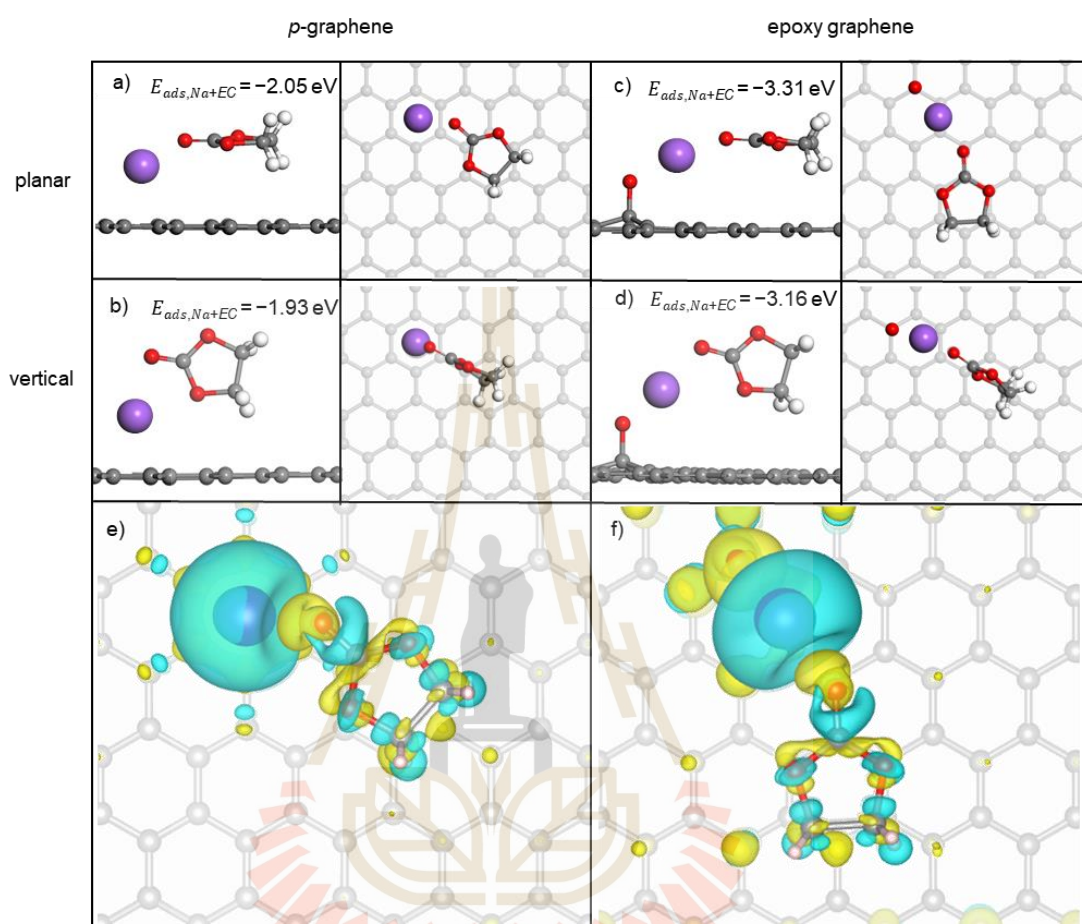
Figure 3.2 Optimized structures of Na and EC co-adsorption which EC molecule oriented planar and vertically on *p*-graphene ((a), (c)) and epoxy graphene ((b), (d)). In ((e) and (f)), the charge density difference of adsorbed EC with planar orientation and Na on the surfaces. Yellow and blue represent an accumulation and depletion of charge, respectively (isosurface value is 0.0015 eV $Å^{-3}$).

3.3 The possible pathways of EC decomposition reactions

The possible pathways of EC decomposition reactions shown in Figure 3.3 were considered (Kumar *et al.*, 2016; Liu *et al.*, 2017). The name of each route was identified

by its final products. As seen in Figure 3.3, the CO route requires the cleavage of one C_C-O_E bond resulting in oC_c ring-opening intermediate. The breaking of the second C_C-O_E bond yields CO gas and $C_2H_4O_2^{2-}$ ion. For the CO_3 route, CO_3 and C_2H_2 gas form via the cleavage of both C_E-O_E bonds through oC_E intermediate. Both intermediates, oC_c and oC_E, can lead to the CO_2 route via breaking C_E-O_E bond of oC_C intermediate and C_C-O_E bond of oC_E intermediate yielding CO_2 and three different side product which can be CH_2OCH_2 (CO_2-1 route), C_2H_4O (CO_2-2 route), or CH_3CHO (CO_2-3 route). We label the CO, CO_2 and CO_3 as product 1, and the other products as product 2.
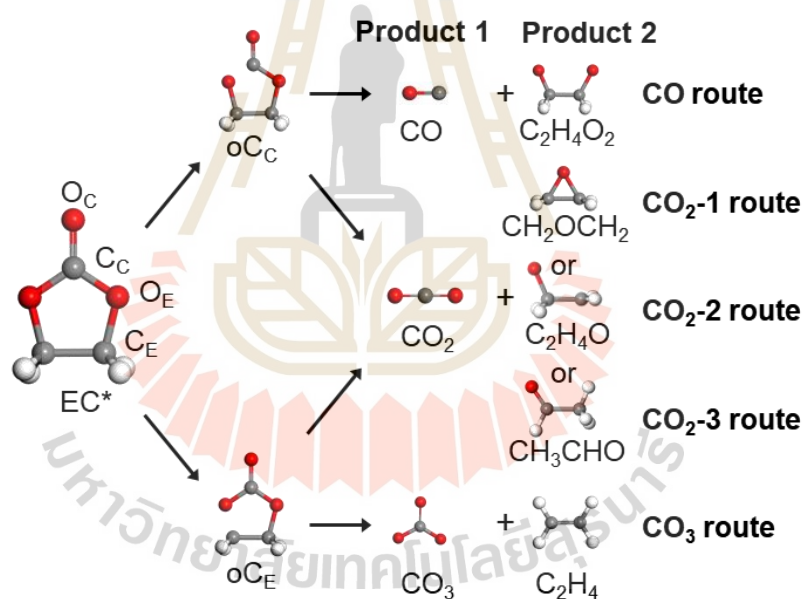
Figure 3.3 Schematic of the proposed EC decomposition routes including CO, CO_2-1, CO_2-2, CO_2-3, and CO_3 routes named with their corresponding final products.

3.4 Decomposition mechanisms of EC with 1 Na atom on *p*-graphene

To investigate the role of epoxy group on the decomposition mechanisms of EC, we constructed reaction energy profiles of the proposed mechanisms on *p*-graphene

and epoxy graphene as shown in Figure 3.4(a) and 3.4(b), respectively. The decomposition of EC molecule begins with the ring-opening reaction at either C_E–O_E or C_C–O_E bonds. The cleavage of C_E–O_E associated with O_E atom move closer to the Na ion leading to the formation of EC ring opening structure at C_E–O_E bond (named as oC_E) with total charge of 0.89 e^- transfer from graphene sheet to the EC molecule (see Figure 3.4(c) and Table 3.1). This process needs to overcome an energy barrier of 0.75 eV and is endothermic by 0.57 eV. From this intermediate, three different routes can occur including CO_3 route, CO_2-1 route, and CO_2-3 route. For the CO_3 route, the breaking of second C_E–O_E bond with the energy barrier of 0.59 eV forms CO_3^- and C_2H_4. If the second bond that cleavage is C_C–O_E bond, producing CO_2 and ethylene oxide (CO_2-1 route) or acetaldehyde (CO_2-3 route). The CO_2-1 route exhibit reaction barrier of 0.85 eV which is higher than that of CO_3 route, while the product is more stable by 0.17 eV. The products of CO_2-3 is the most stable product with the exothermic reaction energy of −1.08 eV. However, the transition state of acetaldehyde formation involves the displacement of hydrogen atom from one C_E atom to another C_E atom with an energy barrier of 1.27 eV which is significantly higher than that in CO_2-1 route CO_3 route (see Figure 3.4(c)). It was found on both CO_2-1 and CO_2-3 routes that 0.82 e^- from oC_E intermediate transfer back to the p-graphene producing negatively charged p-graphene where all final products are neutral.

When the ring-opening reaction of EC was initiated by C_C–O_E bond, the oC_C intermediate was formed and it is significantly less stable than the oC_E intermediate (Figure 3.4(a)). The initial C_C–O_E bond breaking possesses substantially higher reaction energy (1.99 eV) and energy barrier (2.14 eV) than those of the initial C_E–O_E bond-breaking. Three possible routes can proceed through oC_C intermediate (CO, CO_2-1 and

CO_2-3 routes). In CO route, the following cleavage of the second C_C–O_E bond leads to simultaneously C_E–C_E bond dissociation generating formaldehyde and carbon monoxide (see Figure 3.4(c)). Upon EC dissociation, electrons transfer back to graphene sheet similar to the carbon dioxide formation path. Furthermore, the breaking of C_E–O_E bond gives carbon dioxide and acetaldehyde products as same as the products obtained from the pathway through oC_E intermediate (Figure 3.4(c)).

From the reaction profile on p-graphene, the results indicate that the reaction paths with firstly C_E–O_E bond breaking producing oC_E intermediate is more favorable than C_C–O_E bond breaking and is rate-determining step for CO_3 route. On contrary, the breaking of C_C–O_E for CO_2-1 route and H-displacement process of CO_2-3 route are rate determining step. The oC_E intermediate can further react with EC molecule or ring-opening EC yielding sodium butylene carbonate and sodium ethylene carbonate which is observed organic compound in SEI. CO_3 and ethylene product of CO_3 route should be possible products that can be formed due to the most kinetically favorable and these two products are generally observed in SEI on SIBs. Another product is poly(ethylene oxide) that can be form by polymerization of ethylene oxide product from CO_2-1 route. Although CO_2-3 route is the most energetically favorable route, the substantially higher energy barrier for H-displacement for acetaldehyde formation might inhibited the reaction going through this route.

3.5 Decomposition mechanisms of EC with 1 Na atom on epoxy graphene

A similar trend of the energy profiles of all considered decomposition mechanisms was found on the epoxy graphene where the CO_2-3 route is the most energetically favorable

route and CO_3 route is the most kinetically favorable route (Figure 3.4(b)). However, the rate-determining step of EC decomposition is the first bond breaking process where the reaction barrier for C_E–O_E bond cleavage is approximately two times higher than that on graphene which might hinder the EC decomposition reaction. In addition, the CO_2-1 and CO_2-3 routes on epoxy graphene exhibit same energy barrier of 1.02 eV and the difference of energy barrier between CO_3 (0.76 eV) and CO_2-3 routes (1.02 eV) is smaller compare to that on *p*-graphene. These results indicated that the presence of epoxy group on graphene sheet may diminish the rate of EC decomposition.

Table 3.1 Bader charges (in e^-) on graphene sheet (C_{tot}), each final product, each atom of EC molecule and entire EC molecule for each intermediate in 1Na system.

					1 Na						
					p-graphene						
	Na	C_{tot}	C_C	C_E1	C_E2	O_C	O_E1	O_E2	EC(total)	product 1	product 2	O_{epoxy}
EC*	0.91	-0.90	2.14	0.24	0.31	-0.94	-1.14	-1.05	-0.01	-	-	-
oC_E	0.90	0.00	2.09	-0.11	0.38	-1.01	-1.21	-1.26	-0.89	-	-	-
CO_3	0.89	0.08	3.05	-0.22	0.03	-1.39	-1.39	-1.25	-0.97	-0.97	0.00	-
CO_2-1	0.90	-0.82	2.02	-0.14	0.91	-0.98	-1.05	-1.18	-0.08	-0.01	-0.07	-
CO_2-3	0.90	-0.90	2.14	0.28	0.30	-1.03	-1.11	-0.97	0.00	-0.01	0.01	-
oC_C	0.90	-0.03	1.51	0.62	0.24	-1.11	-1.26	-1.01	-0.87	-	-	-
CO	0.90	-0.42	1.14	0.75	0.81	-1.15	-1.14	-1.14	-0.49	-0.01	-0.48	-
					epoxy-graphene						
	Na	C_{tot}	C_C	C_E1	C_E2	O_C	O_E1	O_E2	EC(total)	product 1	product 2	O_{epoxy}
EC*	0.90	0.22	2.09	0.32	0.33	-1.13	-1.01	-1.04	-0.01	-	-	-1.11
oC_E	0.89	0.86	2.06	-0.16	0.40	-1.22	-1.23	-1.00	-0.90	-	-	-0.86
CO_3	0.89	0.89	2.14	-0.17	-0.02	-1.06	-1.07	-0.95	-0.94	-0.94	0.00	-0.85
CO_2-1	0.90	0.24	2.09	-0.16	0.89	-1.02	-1.08	-1.15	-0.02	-0.01	-0.01	-1.12
CO_2-3	0.89	0.21	2.10	0.28	0.33	-1.10	-0.94	-1.01	-0.01	0.06	-0.06	-1.10
oC_C	0.89	0.76	1.52	0.64	0.20	-1.01	-1.20	-1.11	-0.82	-	-	-0.83
CO	0.89	0.24	1.07	0.83	0.85	-1.09	-1.09	-1.07	-0.07	-0.01	-0.06	-1.07

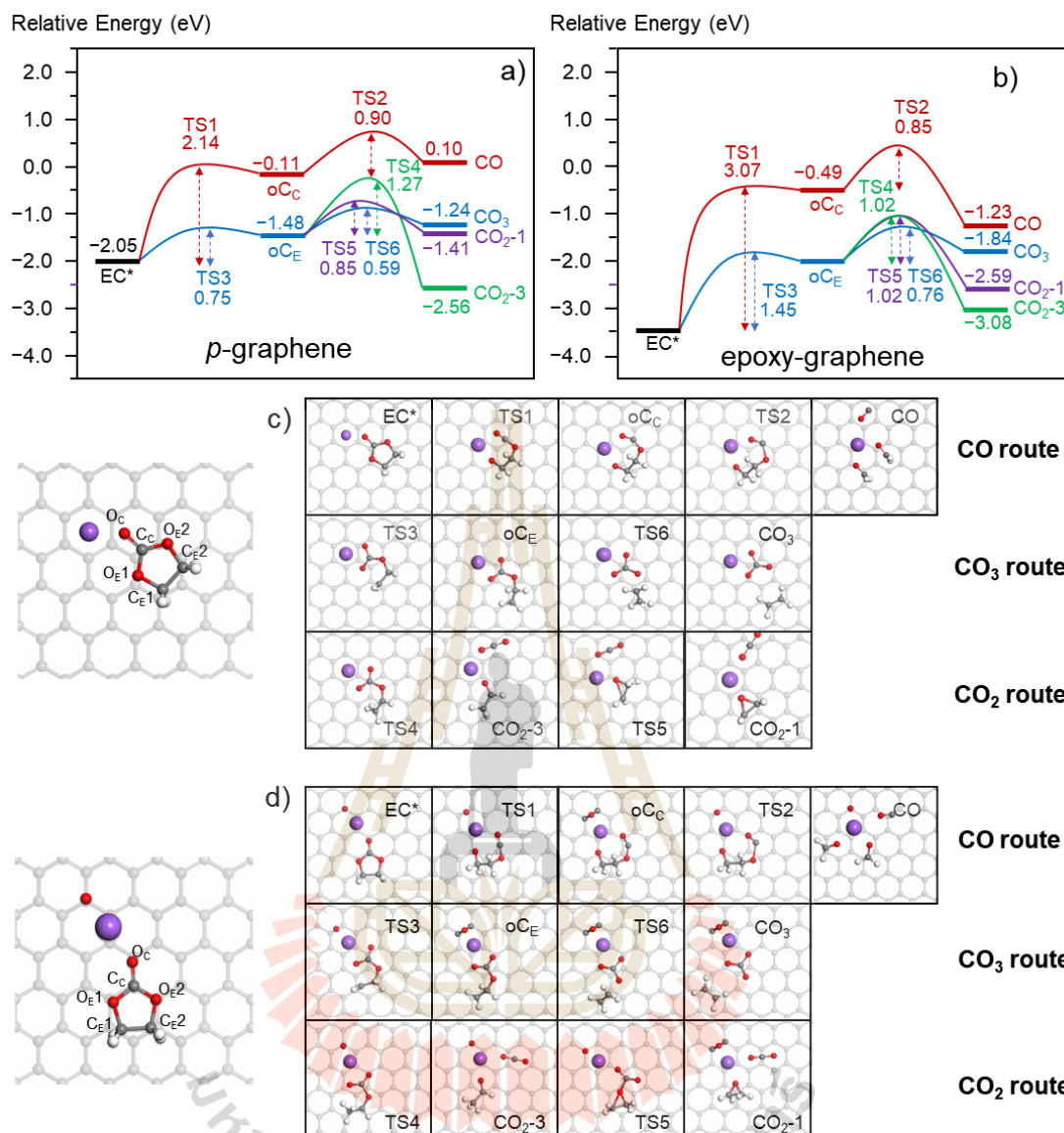**Figure 3.4** Reaction energy profiles for the EC decomposition on (a) *p*-graphene and (b) epoxy graphene. The relative energies and energy barriers for all intermediates and transition states are also shown along the pathways. The corresponding intermediates and transition states structures of EC decomposition reactions on (c) *p*-graphene and (d) epoxy graphene. Purple: Na; Grey: C; red: O; white: H.

3.6 References

Diklić, N. P., Dobrota, A. S., Pašti, I. A., Mentus, S. V., Johansson, B., and Skorodumova, N. V. (2019). Sodium storage via single epoxy group on graphene – The role of surface doping. **Electrochim. Acta**. 297: 523.

Kumar, H., Detsi, E., Abraham, D. P., and Shenoy, V. B. (2016). Fundamental Mechanisms of Solvent Decomposition Involved in Solid-Electrolyte Interphase Formation in Sodium Ion Batteries. **Chem. Mater.** 28: 8930.

Liang, Z., Fan, X., Zheng, W., and Singh, D. J. (2017). Adsorption and Formation of Small Na Clusters on Pristine and Double-Vacancy Graphene for Anodes of Na-Ion Batteries. **ACS Appl. Mater. Interfaces**. 9: 17076.

Liu, Q., Mu, D., Wu, B., Wang, L., Gai, L., and Wu, F. (2017). Density Functional Theory Research into the Reduction Mechanism for the Solvent/Additive in a Sodium-Ion Battery. **ChemSusChem**. 10: 786.

Olsson, E., Chai, G., Dove, M., and Cai, Q. (2019). Adsorption and migration of alkali metals (Li, Na, and K) on pristine and defective graphene surfaces. **Nanoscale**. 11: 5274.

Pašti, I. A., Jovanović, A., Dobrota, A. S., Mentus, S. V., Johansson, B., and Skorodumova, N. V. (2018). Atomic adsorption on pristine graphene along the Periodic Table of Elements – From PBE to non-local functionals. **Appl. Surf. Sci.** 436: 433.

CHAPTER IV

ETHYLENE CARBONATE DECOMPOSITION WITH 2 Na ATOMS ON *P*-GRAPHENE AND EPOXY GRAPHENE SURFACES

4.1 Co-adsorption of 2 Na atoms and EC molecule on p-graphene and epoxy graphene

To investigate the decomposition mechanism of EC molecule in higher sodium concentration, we introduced one more Na atom on the *p*-graphene and epoxy graphene and referred as 2Na system. In the *p*-graphene case, the additional Na atom tends to locate close to another Na atom with a stable distance of 3.46 Å causing a slight shift of each Na atom from the center of hollow sites (Figure 4.1(a)) with an $E_{ads,Na}$ of -1.64 eV. The charge analysis results in Figure 4.1(a) show that *p*-graphene only receive about 1.00 e$^-$ from Na atoms while charge of 0.74 e$^-$ located on the Na atom close to C_C atom and 0.35 e$^-$ located on the other Na atom. In the presence of epoxy, the added Na atom interact with the epoxy group through electrostatic interaction and exhibit two times lower $E_{ads,Na}$ (-4.53) than the 1Na system. On this surface, the added Na atoms loss 0.89 e$^-$ as same as another Na atom where the graphene sheet receives 0.75 e$^-$ (total charge of -0.50 e$^-$) and while the rest were transferred to the epoxy group (total charge of -1.23 e$^-$). The adsorption of EC molecules onto these systems show similar result that the planar orientation is more stable than the vertical one. In addition, an O_E atom

of the EC preferentially binds with the added Na atom which its bond length is longer

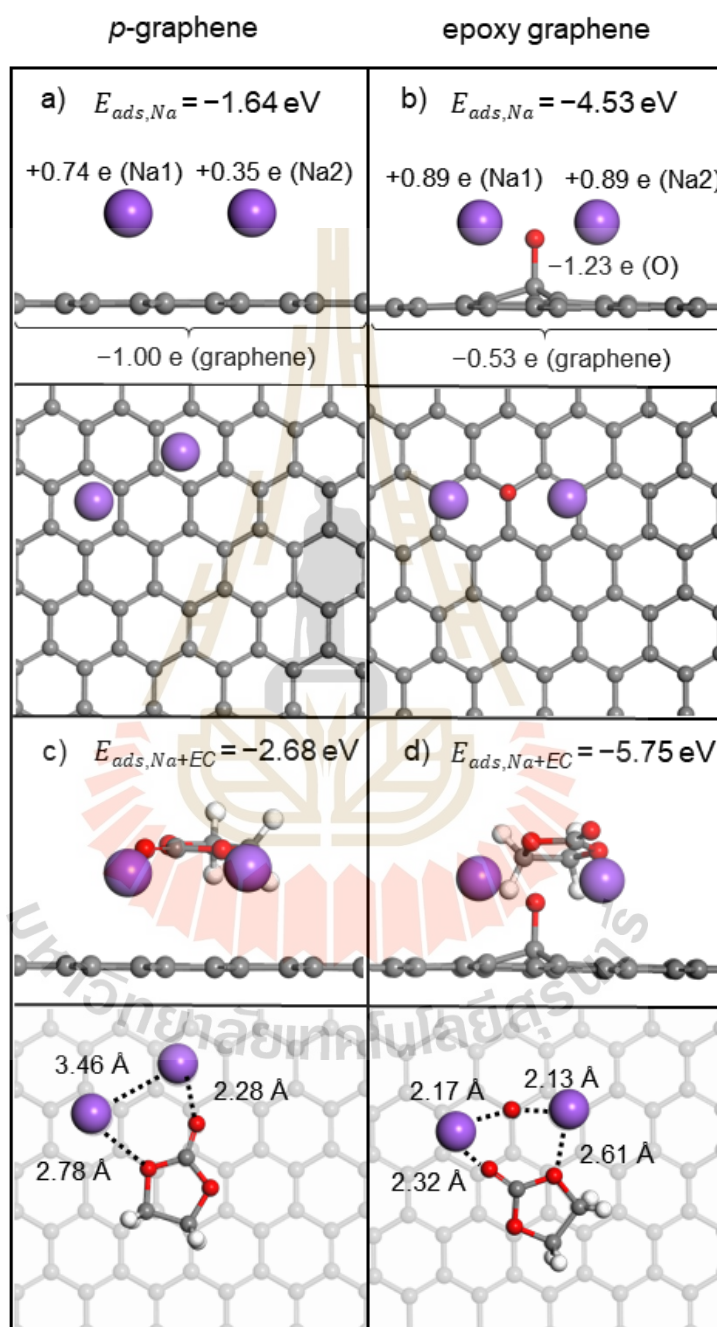than that of Na−O_C bond (Figure 4.1(c) and (d)).

Figure 4.1 Optimized structures of 2 Na atoms and EC molecule co-adsorption on *p*-graphene (a) and epoxy graphene (b).

4.2 Decomposition mechanisms of EC with 2 Na atoms on *p*-graphene

For the CO_3 route in this system, two $C_E - O_E$ bonds simultaneously break without reaction barrier to produce Na_2CO_3 and ethylene gas (Figure 4.2(a)). This is due to the electron can directly transfer from Na atoms to EC molecule especially the one that located close to O_E atom of EC molecule. Additionally, the CO_3 route is exothermic by -2.37 eV which can be attributed to the stabilization of CO_3^{2-} product by 2 positively charged Na^+ ions forming Na_2CO_3. A stable oC_E intermediate cannot be found in this system due to simultaneous cleavage of both $C_E - O_E$ bonds. However, in CO route, the first $C_C - O_E$ bond breaking process can form oC_C intermediate with reaction barrier of 0.54 eV. The step is endothermic with a small reaction energy of 0.17 eV which is about three times lower than that in 1 Na system. The second $C_C - O_E$ bond breaking step is also endothermic reaction with higher reaction barrier (0.43 eV) and reaction energy (0.47 eV). Unlike the CO route in the 1 Na system, the second $C_C - O_E$ bond cleavage produces $C_2H_4O_2$ and the C−C bond does not break to form formaldehyde. Differently from 1 Na system, the product of C_2H_4O in CO_2-2 route is more likely to form than ethylene oxide in CO_2-1 route due to the structural transformation from ethylene oxide to C_2H_4O during the energy minimization. The C_2H_4O product occurs by breaking of $C_E - O_E$ bond of oC_C intermediate with the reaction energy of -0.4 eV, and the corresponding barrier of 1.29 eV. Unlike 1Na system, both CO_3 and CO_2 route were exothermic and the CO_3 route shows significantly lower reaction energy than the CO_2 route by 1.83 eV. Therefore, the CO_3 route for 2Na system on *p*-graphene is the most thermodynamically and kinetically favorable.

4.3 Decomposition mechanisms of EC with 2 Na atoms on epoxy graphene

When the epoxy group presents on the surface, the reaction energies and reaction barriers of EC decomposition for most route is quite similar to that of 1 Na system on p-graphene. As can be clearly seen from Figure 4.2(b), all possible decomposition routes except for CO_2-3 route on this surface are endothermic Differently, the reaction barrier requires for the CO_3 route from is higher than that of both possible CO_2 routes because the repulsion between the O_C atom of EC molecule and epoxy group, as displayed in Figure 4.2(d). Therefore, the CO_2-3 route is remained the most energetically favorable route whereas the CO_2-1 route is more kinetically favorable but with the reaction barrier slightly lower than CO_2-3 route by 0.08 eV. According to Table 4.1, CO_3 product for CO_3 route can receive only -1.18 e^- from the graphene sheet due to the charge of graphene sheet is consumed by epoxy group and is not likely to transfer to EC molecule.

Table 4.1 Bader charges (in e^-) on graphene sheet (C_{tot}), each final product, each atom of EC molecule and entire EC molecule for each intermediate in 2Na system.

	Na1	Na2	C_{tot}	C_C	C_E1	C_E2	O_C	O_E1	O_E2	EC(total)	product 1	product 2	O_{epoxy}
						2 Na							
						p-graphene							
EC*	0.35	0.74	-1.00	2.12	0.31	0.35	-1.23	-1.08	-1.01	-0.09	-	-	-
CO_3	0.88	0.88	-0.06	2.04	-0.19	-0.02	-1.27	-1.24	-1.22	-1.71	-1.70	-0.01	-
CO_2-2	0.89	0.88	-0.41	1.43	0.47	0.32	-1.28	-1.25	-1.20	-1.36	-	-	-
CO_2-3	0.88	0.88	-0.27	1.13	0.45	0.56	-1.15	-1.25	-1.13	-1.49	-0.02	-1.47	-
oC_C	0.89	0.86	-0.88	2.12	0.41	-0.21	-1.06	-1.18	-1.07	-0.87	-0.02	-0.86	-
CO	0.90	0.89	-1.07	2.10	0.57	-0.10	-1.11	-1.25	-1.00	-0.71	-0.02	-0.70	-
						epoxy-graphene							
	Na1	Na2	C_{tot}	C_C	C_E1	C_E2	O_C	O_E1	O_E2	EC(total)	product 1	product 2	O_{epoxy}
EC*	0.89	0.89	-0.53	2.10	0.39	0.33	-1.18	-1.04	-1.04	-0.02			-1.23
oC_E	0.89	0.89	0.31	2.07	0.36	-0.24	-1.25	-1.02	-1.20	-0.90			-1.19
CO_3	0.89	0.89	0.55	2.12	-0.36	0.03	-1.13	-1.09	-1.09	-1.18	-1.18	0.00	-1.15
CO_2-1	0.88	0.88	-0.54	3.75	0.26	0.20	-1.90	-0.94	-1.86	-0.01	-0.01	0.00	-1.21
CO_2-3	0.89	0.88	-0.56	2.28	0.76	-0.17	-1.61	-1.00	-0.69	-0.03	-0.02	-0.02	-1.18
oC_C	0.89	0.88	0.22	1.49	0.61	0.29	-1.07	-1.27	-1.04	-0.88			-1.11
CO	0.89	0.88	0.24	1.13	0.58	0.62	-1.13	-1.20	-1.09	-0.90	0.00	-0.89	-1.11

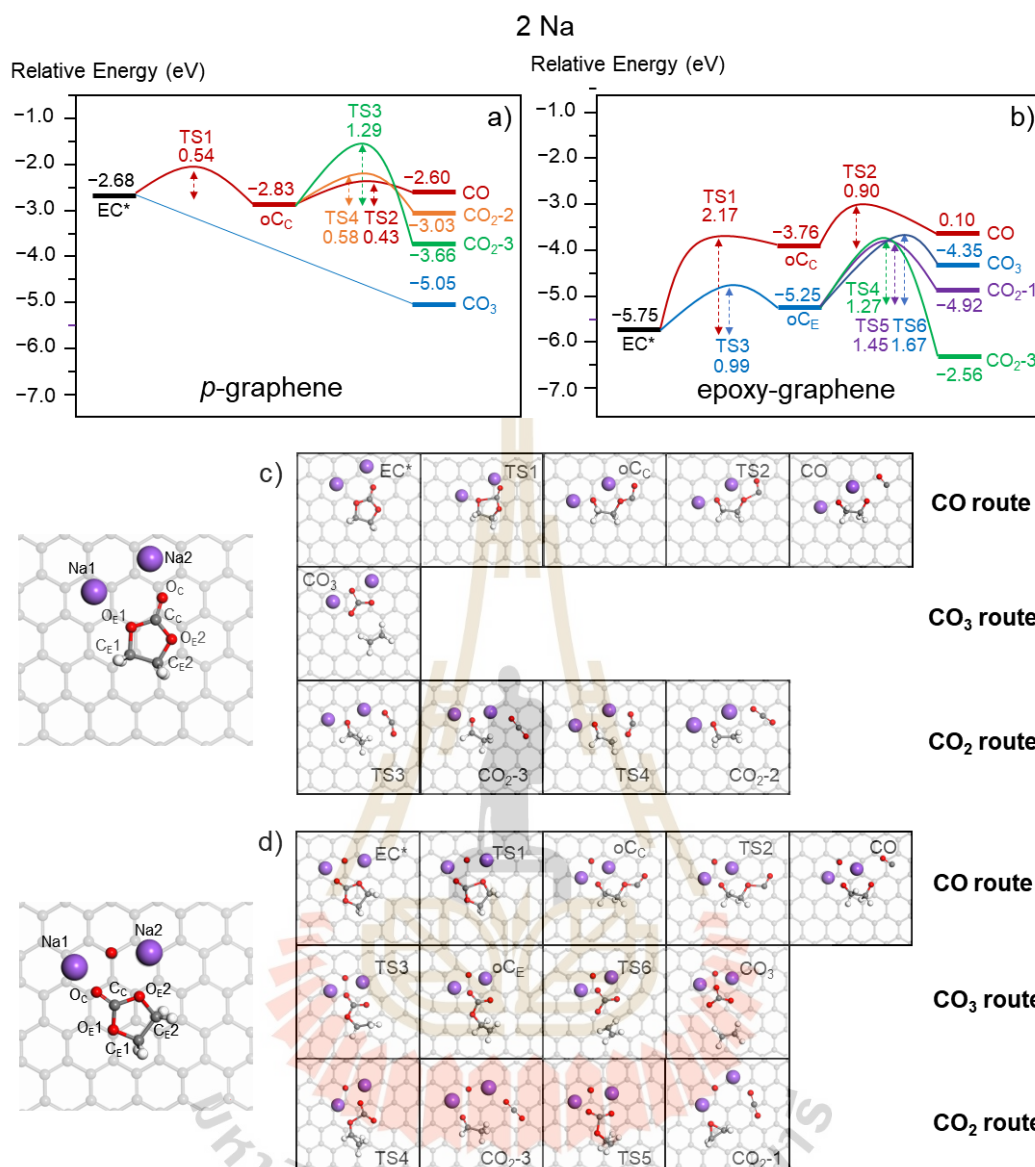**Figure 4.2** Reaction energy profiles for the EC decomposition reactions with 2 Na atoms on (a) *p*-graphene and (b) epoxy graphene. The relative energies and energy barriers for all intermediates and transition states are also shown along the pathways. The corresponding intermediates and transition states structures of EC decomposition reactions on (c) *p*-graphene and (d) epoxy graphene. Purple: Na; Grey: C; red: O; white: H.

CHAPTER V

SOLVATION EFFECT ON ETHYLENE CARBONATE

DECOMPOSITION MECHANISM

5.1   Co-adsorption of Na atom and EC molecules in solvent environment.

Previous studies have proposed that the inclusion of electrolyte environment play a crucial role on electrolyte decomposition mechanisms which can account for the local interaction between EC molecules (Xu *et al.*, 2017; Young and Smeu, 2018). In order to investigate the role of solvent environment, we stepwise increase the number of EC molecules from 1 molecule to 6 molecules and calculated the adsorption energies corresponding to the following equation (3):

$$E_{ads,Na+(EC)_n} = E_{Epoxy(Graphene)+Na+(EC)_n} - (E_{Epoxy(Graphene)} + E_{Na} + n \times E_{EC}) \qquad (3)$$

where $E_{Epoxy(Graphene)+Na+(EC)_n}$ is the total energy of n EC molecules and Na adsorption on graphene or epoxy graphene, $E_{Epoxy(Graphene)}$ is the total energy of the graphene or epoxy graphene sheet; E_{Na} is the total energy of an isolated Na atom; E_{EC} is the total energy of an isolated EC molecule, and *n* is the number of EC molecules.

The plot between adsorption energies and number of the molecules and the corresponding solvation structure are shown in Figure 5.1 From the graph, the change in adsorption energy is slightly decrease when increase the number of the molecules from 5 to 6 molecules indicated that the solvation shell of 5 molecules gives the most stable configurations. The 6 EC molecules solvation structures show that the 6th

EC molecule weakly interact with Na ion through its O_E atom with further distance of 3.6 Å. The 5 molecules solvation structure is in agreement with the previous experimental work reported that the preferential oxygen coordination number of Na ion in pure EC is $\sim$5 (Kamath *et al.*, 2014). Thus, the effects of electrolyte environment (only for the first solvation shell of Na ion) are studied explicitly by adding 5 EC molecules into the systems and labelled each molecule by EC1, EC2, EC3, EC4, and EC5. However, to avoid spurious interactions between periodic images causing by the inclusion of solvation structures, the cell size of single-layer graphene was increased to 8×8 supercell together with expanding of vacuum gap to 26 Å .

On *p*-graphene, four EC molecules, EC1, EC2, EC3, and EC4, tend to interact with Na ion through O_c atoms with an average distance of 2.34 Å forming a planar structure surrounding the Na ion (Figure 5.2(a)). The EC5 molecule located above the square planar $Na^+(EC)_4$ complex interacts with Na ion through O_E atoms with bond distance of 2.82 Å. This molecule oriented in a way that maximize the hydrogen bond interactions with the other EC molecules.

On epoxy graphene, EC molecules cannot form a perfect square planar $Na^+(EC)_4$ complex because of the repulsion between oxygen atoms of EC molecules and epoxy group. Hence, the two EC molecules near epoxy group (EC1 and EC4) slightly point their O_C and O_E upward while hydrogen atoms of these molecules bend toward epoxy group as seen in Figure 5.2(b).
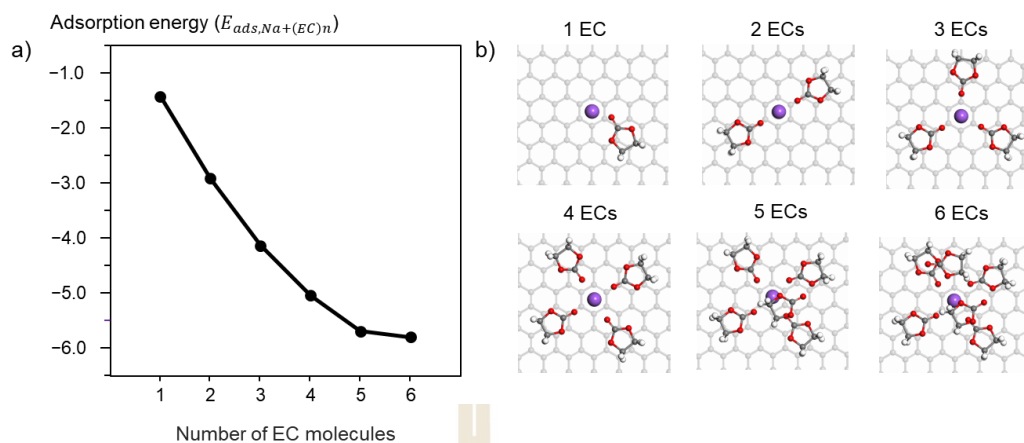
Figure 5.1 a) The change of adsorption energy per number of EC molecule ($E_{ads,Na+(EC)n}$) with the increasing of EC molecules and b) the corresponding solvation structures.
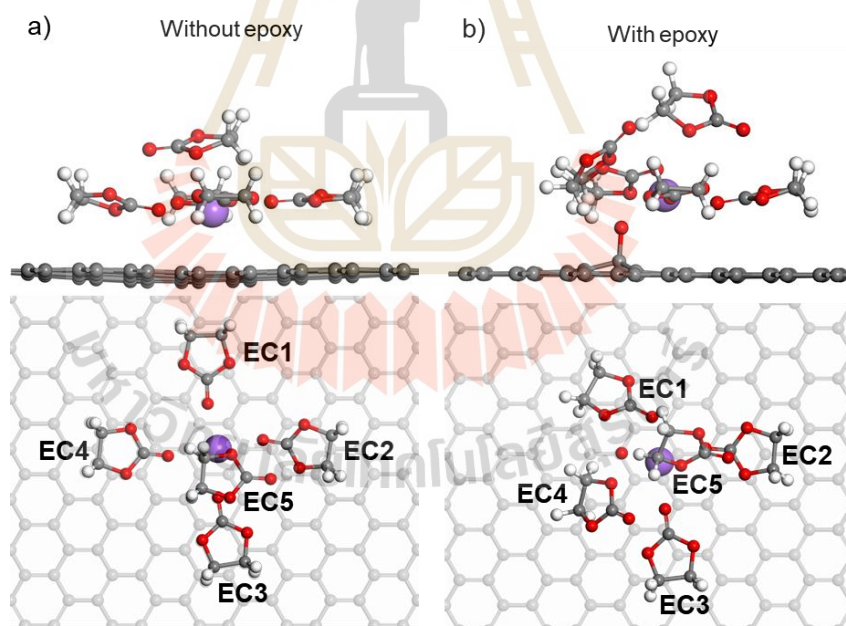

Figure 5.2 Optimized solvation structures of 5 EC molecules on a) *p*-graphene and b) epoxy graphene.

5.2 Decomposition mechanisms of EC in a solvent environment on *p*-graphene and epoxy graphene

To investigate the effect of the electrolyte solvation on reaction pathways, the reaction energies of the five EC decomposition pathways including explicit model of EC solvation shell were computed. Because there are total 5 EC molecule on the surfaces, we investigated the decomposition mechanisms of only one EC molecule that exhibit the longest $C_C - O_E$ and $C_E - O_E$ bond distances which correspond to the highest degree of bond activation. The EC4 molecule on both *p*-graphene and epoxy graphene shows the longest $C_C - O_E$ and $C_E - O_E$ bond distances (Figure 5.3a and 5.3b), and thus was chosen to study the decomposition mechanism.

In *p*-graphene system, decomposition of EC molecule follows the same trend as the system without electrolyte environment. However, all steps especially the first bond breaking steps exhibit nearly two times higher reaction energies (2.72 eV for $C_C - O_E$ bond and 1.21 eV for $C_E - O_E$ bond) than that without the inclusion of EC solvation shell as shown in Figure 5.3. These reaction energies are even higher than the reaction barrier of the first bond breaking in the system with 1 EC molecule. EC molecule is stabilized by the other EC molecules in the solvation shell, thus higher reaction energies are required for EC decomposition. Similar results were also found on epoxy graphene that the electrolyte environment increase the reaction energies and reaction barriers for EC decomposition reaction. For these pathways, the same behavior of epoxy group was found that it consumes the charge from graphene sheet and suppress the EC decomposition reaction.
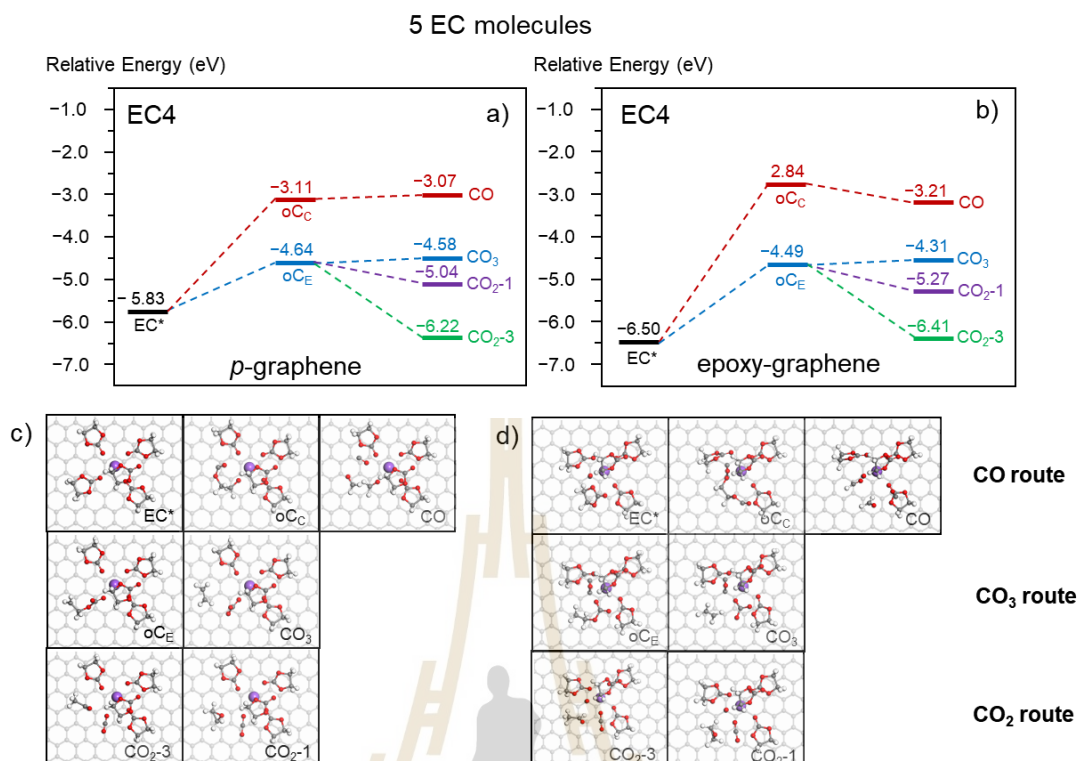
Figure 5.3 Reaction energy profiles for the EC decomposition reactions with the inclusion of solvent environment on (a) *p*-graphene and (b) epoxy graphene. The relative energies and energy barriers for all intermediates and transition states are also shown along the pathways. The corresponding intermediates of EC decomposition reactions on (c) *p*-graphene and (d) epoxy graphene. Purple: Na; Grey: C; red: O; white: H.

Apart from previously mentioned mechanisms, as can be clearly seen in Figure 5.4, we found that epoxy group can chemically interact with EC molecule by two mechanisms which are deprotonation of EC to form hydroxyl group during ring-opening process or O epoxy dissociation from the graphene sheet to bond with EC molecule. When deprotonation occurs during the first bond breaking reaction, the ring opening intermediates oC_E was stabilized, and the reaction energies are significantly decrease (Figure 5.4(c)). This intermediate is then cleaving the C_C-O_E bond producing

CO_2 and $OCHCH_2$ product with overall slightly exothermic reaction energy (Figure 5.4(d). Furthermore, the C−O bond between graphene sheet and epoxy group can be break results in the reconstruction of graphene sheet to become planar and O^- that can attack the EC molecule and induce the decomposition (Figure 5.4(e)). Both ring-opening intermediate and final products of this route are more stable than that of H abstraction route. The intermediate formed via epoxy dissociation is further reduced to form CO_3 and acetaldehyde with more exothermic reaction energy than the other routes. This suggests the importance of explicit solvation model that can have a major influence on the decomposition reaction mechanism. The difference pathways possibly take place and reaction energies results significantly change.

Table 5.1 Bader charges (in e^-) on graphene sheet (C_{tot}), each final product, each atom of EC molecule and entire EC molecule for each intermediate in 5 ECs system.

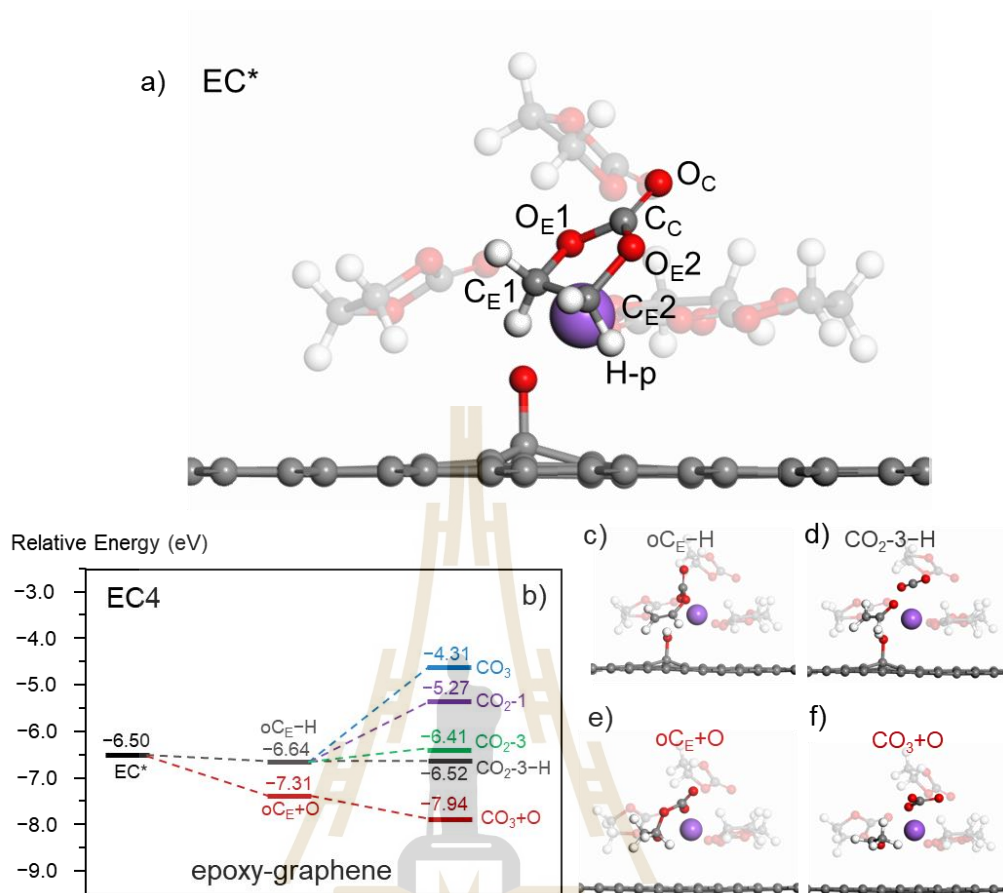|	Na	C_{tot}	C_C	C_E1	C_E2	O_C	O_E1	O_E2	H-p	EC(total)	product 1	product 2	Oepoxy
EC*	0.90	0.22	2.09	0.32	0.33	-1.13	-1.01	-1.04	-0.01				-1.11
oC_E−H	0.90	0.48	2.07	-0.16	0.49	-1.21	-1.20	-1.01	0.61	-0.87			-1.10
CO_2-3−H	0.90	0.03	2.09	0.75	-0.22	-1.06	-1.07	-1.07	0.58	-0.42	-0.04	-0.38	-1.07
oC_E+O	0.90	0.04	2.11	0.36	0.60	-1.10	-1.02	-1.11	0.02	-0.91			-0.93
CO_3+O	0.90	0.04	2.16	0.89	-0.16	-0.98	-1.00	-1.10	0.05	-0.92	-0.91	-0.01	-1.12

Figure 5.4 Reaction energy profiles for the EC decomposition reactions with the inclusion of solvent environment that epoxy group chemically interact with the EC molecule on epoxy graphene: (a) initial adsorption configuration for 5 EC molecules on epoxy graphene. (b) Reaction energy profiles for the EC decomposition reactions. (c)-(d) corresponding structures of intermediates. The relative energies for all intermediates and transition states are also shown along the pathways. The corresponding intermediates of EC decomposition reactions. Purple: Na; Grey: C; red: O; white: H.

5.3   References

Kamath, G., Cutler, R. W., Deshmukh, S. A., Shakourian-Fard, M., Parrish, R.,
Huether, J., Butt, D. P., Xiong, H., and Sankaranarayanan, S. K. R. S. (2014).
In Silico Based Rank-Order Determination and Experiments on Nonaqueous
Electrolytes for Sodium Ion Battery Applications. **J. Phys. Chem. C**. 118:
13406.

Xu, S., Luo, G., Jacobs, R., Fang, S., Mahanthappa, M. K., Hamers, R. J., and Morgan,
D. (2017). Ab Initio Modeling of Electrolyte Molecule Ethylene Carbonate
Decomposition Reaction on Li(Ni,Mn,Co)O$_2$ Cathode Surface. **ACS Appl.
Mater. Interfaces**. 9: 20545.

Young, J., and Smeu, M. (2018). Ethylene Carbonate-Based Electrolyte Decomposition
and Solid-Electrolyte Interphase Formation on Ca Metal Anodes. **J. Phys.
Chem. Lett.** 9: 3295.

CHAPTER VI

CONCLUSIONS

Using first principles calculations, we explored the mechanism of ethylene carbonate decomposition on the *p*-graphene and epoxy graphene surfaces to study the role of epoxy functional group. Our calculations were carried out under three different system consisting of 1Na system, 2Na system, and 5 EC molecules system. The results indicated that the CO_3 route is kinetically favorable route with the first-bond breaking step is rate-determining step whereas the CO_2-3 route is the most energetically favorable pathway on *p*-graphene, but the significant higher energy barrier (two times higher than that of CO_3 route)is required for H-displacement process in order to produce acetaldehyde. The presence of epoxy group does not change the trend for EC decomposition routes, but it increases reaction energies and reaction barriers for all steps. This can be explained by graphene electron deficiency which results from the epoxy group withdraws electrons from graphene surface. This decreases the ability of the graphene surface to reduce EC molecule. The increase of sodium concentration also shows different results that the CO_3 route become more kinetically and energetically favorable because of the strong electrostatic interaction between two Na ion and CO_3^{2-} ion to form Na_2CO_3. The presence of epoxy in 2Na system also shows the similar role of epoxy that it withdraw about 1 e^- from the graphene sheet which hinder the reduction of EC molecule. Moreover, the important of explicit solvent model by including the first EC solvation shell structure in the model was investigated. The hydrogen bonds among EC molecules were maximized

and EC molecules were stabilized. Therefore, the solvent environment was found to increase the reaction energies of each route. More importantly, the inclusion of solvent environment results in various EC orientations around the epoxy group and difference mechanisms can be found. Additional two mechanisms were found 1) deprotonation of EC molecule and 2) O epoxy dissociation that remove the epoxy group from the surface and bond forming between C_E atom of EC molecule and the dissociated O. These mechanism substantially lower the reaction energies of EC decomposition reaction which is also lower than EC decomposition on epoxy graphene with 2Na system. Therefore, we may conclude that the epoxy group on carbon-based materials have two different roles. The first role happens when the epoxy is not directly contact with EC molecule. In this way, the presence of epoxy on the basal plane will consume electrons from the graphene sheet and decrease the ability of the graphene to reduce the EC molecule compared with the surface without epoxy group. When we include the electrolyte environment into our system, the EC molecule reorganize to a certain orientation where it can chemically interact with epoxy group. The interaction between them shown more favorability compared with that without this interaction. Thus, the presence of epoxy group on carbon-based anode surface might both inhibit or accelerate the decomposition of EC molecule depending on the position of itself whether it allow for the interaction between them or not. This could explain the reason why the carbon anodes with more surface area result in more irreversible capacity loss. Our calculations also show the important of explicit solvent on the decomposition mechanisms that not only change the reaction energies of the reactions but also lead to totally different decomposition mechanisms. Furthermore, other effect including morphology, edge functional groups, defects, salt anions, and additives may be addressed in future work.
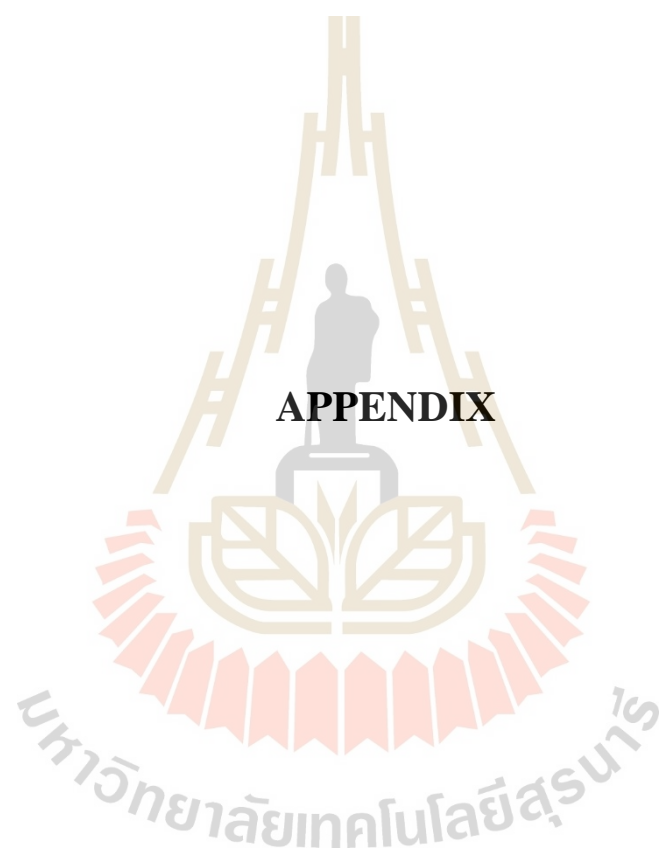
APPENDIX

APPENDIX

PUBLICATION AND PRESENTATIONS

A.1 List of presentations (oral)

Watthaisong, P., Suthirakun, S., and Hirunsit, P. (January 2019). Theoretical Studies of Epoxy Group Effect on Ethylene Carbonate Decomposition on Carbon Anode of Sodium ion Batteries. **The 2nd Taiwan-Thailand-Vietnam Workshop on Theoretical and Computational Chemistry (TTV2)**. Sirindhorn Science Home, Thailand Science Park, Pathum Thani, Thailand.

Theoretical Studies of Epoxy Group Effect on Ethylene Carbonate Decomposition on Carbon Anode of Sodium ion Batteries

Panuwat Watthaisong[1,2], Suwit Suthirakun[1,2]*, and Pussana Hirunsit[3]*

[1]School of Chemistry, Institute of Science, Suranaree University of Technology, Nakhon Ratchasima, 30000, Thailand
[2]Center of Excellence in Advanced Functional Materials, Suranaree University of Technology, Nakhon Ratchasima, 30000, Thailand
[3]National Nanotechnology Center (NANOTEC), National Science and Technology Development Agency (NSTDA), Pathum Thani, 12120, Thailand
*E-mail: suthirak@sut.ac.th (SS) and pussana@nanotec.or.th (PH)

Abstract:

In recent decades, the increasing demand for sustainable energy sources has been substantially driven the demand of energy storages especially lithium-ion batteries (LIBs). Although LIBs have high energy density and good electrochemical properties, they still have challenging questions regarding safety, lifetime, poor low-temperature performance, and the cost of Li due to the uneven distribution and control of Li sources by only a few companies worldwide. Sodium-ion batteries (SIBs) are promising to be an alternative to LIBs owing to sodium is the second lightest and smallest alkali metal and its resources are more abundant and widely distributed. Since chemical properties of sodium are similar to lithium, SIBs also exhibit similar chemical mechanisms to that of LIBs.[1] However, many challenges must be overcome to make NIBs well positioned in commercialization such as low cyclability, and low stability of the solid-electrolyte interphase (SEI) formation, results from the decomposition of organic solvents in the electrolyte on the anode of both LIBs and SIBs. The SEI has a profound effect on cycle life and performance of the batteries.[2] Therefore, understanding the SEI compositions and its formation mechanisms is crucial for NIBs development. Carbon-based anode materials are commonly used as the anode for NIBs because of their appropriate electrochemical properties, an abundance of carbon and safety. The oxygen-containing groups often present in the carbon-based anode and they usually actively involved in chemical reactions. In this work, we performed density functional theory (DFT) calculations and ab initio molecular dynamics (AIMD) simulation to study the effect of epoxy group in graphene oxide on decomposition mechanisms of ethylene carbonate, which is a common solvent used in SIBs. The understanding of solvent decomposition pathways would enable us to gain the insight of SEI formation mechanisms and compositions of the SEI film which could be utilized to determine the SEI stability.
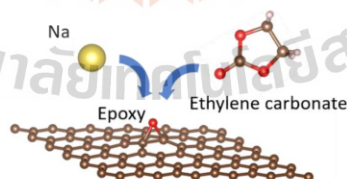
References:
1. J.-Y. Hwang, S.-T. Myung and Y.-K. Sun, **Chemical Society Reviews** *46*, 3529-3614 (2017).
2. P. Verma, P. Maire and P. Novák, **Electrochimica Acta** *55*, 6332-6341 (2010).

CURRICULUM VITAE

Panuwat Watthaisong was born on May 8, 1997 in Nakhon Ratchasima, Thailand. He received his B.Sc. in Chemistry (first-class honors) in 2019 from the School of Chemistry, Institute of Science, Suranaree University of Technology. He has granted the "His Majesty the King's 80th Birthday Anniversary" Scholarship from Suranaree University of Technology since 2014. During his senior year in bachelor's degree, He has successfully completed an internship (4 months) at the Nanocatalysis and Molecular Simulation Research Group of the National Nanotechnology Center (NANOTEC) operating under the National Science and Technology Development Agency (NSTDA, Thailand). In 2019, he continued to pursue the Master's degree program in the School of Chemistry, Suranaree University of Technology with Thailand Graduate Institute of Science and Technology scholarship (TGIST) from National Science and Technology Development Agency (NSTDA, Thailand) under the supervision of Asst. Prof. Dr. Suwit Suthirakun. He has participated in the international conferences (listed in APPENDIX A) during his master program education.